






RESEARCH ARTICLE | JANUARY 26 2023

Computational fluid dynamics investigation of bitumen residues in oil sands tailings transport in an industrial horizontal pipe

Somasekhara Goud Sontti ; Mohsen Sadeghi ; Kaiyu Zhou (周凯宇) ; Enzu Zheng (郑恩祖) ; Xuehua Zhang (张雪花)  

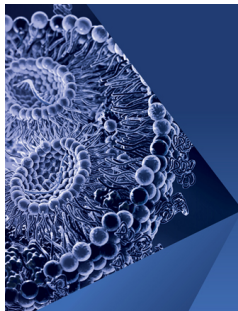


Physics of Fluids 35, 013340 (2023)

<https://doi.org/10.1063/5.0132129>



CrossMark



Physics of Fluids

Special Topic:

Flow and Lipid Nanoparticles

Guest Editors: Richard Braatz and Mona Kanso

[Submit Today!](#)

Computational fluid dynamics investigation of bitumen residues in oil sands tailings transport in an industrial horizontal pipe

Cite as: Phys. Fluids **35**, 013340 (2023); doi: 10.1063/5.0132129

Submitted: 26 October 2022 · Accepted: 21 December 2022 ·

Published Online: 26 January 2023



View Online



Export Citation



CrossMark

Somasekhara Goud Sontti,¹ Mohsen Sadeghi,¹ Kaiyu Zhou (周凯宇),¹ Enzu Zheng (郑恩祖),² and Xuehua Zhang (张雪花)^{1,a)}

AFFILIATIONS

¹Department of Chemical and Materials Engineering, University of Alberta, Edmonton, Alberta T6G 1H9, Canada

²CSIRO Mineral Resources, Clayton, Victoria 3168, Australia

^{a)}Author to whom correspondence should be addressed: xuehua.zhang@ualberta.ca

ABSTRACT

Pipeline transport is commonly used in the oil sand industry to convey crushed oil sand ores and tailings. Bitumen residues in the oil sand tailings can be a threat to the environment that separating them from tailings before disposal is crucial. However, low bitumen concentration in the tailing slurry and the complex transport characteristics of the four-phase mixture make the process difficult. This study establishes an Eulerian–Eulerian (E–E) computational fluid dynamics model for an industrial-scale oil sand tailings pipeline. A comprehensive sensitivity analysis was conducted on the selection of carrier-solid and solid-bitumen drag models. The combination of small and large particle sizes (i.e., 75 and 700 μm) and bitumen droplet size (i.e., 400 μm) provided good agreement with field data in velocity profiles and pressure drop. The validated model was subsequently extended to investigate the influence of the secondary phase (i.e., bitumen droplets and bubbles) on flow characteristics in a tailing pipeline. The investigation covered a range of bitumen droplet size (100–400 μm), bitumen fraction (0.0025–0.1), bubble size (5–1000 μm), and bubble fraction (0.0025–0.3) and their influences on the velocity, solids, and bitumen distribution are revealed. For an optimum bubble size of 500 μm , a maximum recovery of 59% from the top 50% and 83% from the top 75% of the pipe cross section was obtained. The present study demonstrates the preferential distribution of bitumen and provides valuable insight into bitumen recovery from an industrial-scale tailing pipeline.

Published under an exclusive license by AIP Publishing. <https://doi.org/10.1063/5.0132129>

I. INTRODUCTION

Hydraulic pipeline transport of concentrated slurry flows has a wide range of applications in diverse industries, such as mining, chemistry, oil, and waste treatment.^{1,2} Transport of slurry flows by pipeline is considered safe, energy-efficient, and cost-effective. The concentrated slurry flow is a multicomponent system consisting of solid particles, water, and other compounds. Those fine particles smaller than 44 μm along with water form non-Newtonian carrier fluid, which typically exhibits shear-thinning behavior.^{3–5} The presence of coarse particles would form heterogeneous and fully stratified flows due to a low degree of turbulence. It lowers the transport capacity and increases the energy cost simultaneously.^{6–8} In recent decades, many researchers have considerably reported both experimental and numerical studies of slurry transport in horizontal pipelines. Most of the previous works are concerned with a two-phase slurry system, considering a single and multi-size particle slurry system.^{9,10} Regardless, the real world of

industrial-scale slurry systems is complex due to the flow's composition and non-Newtonian behavior.

In the oil sand industry, pipe transport is used to convey crushed oil sand ores and tailings.^{11,12} Both concentrated slurry flows contain bitumen droplets and trace entrapped gas bubbles in addition to solid particles and water. After extraction of liberated bitumen, the concentrated oil sand tailings composed of a tiny fraction of bitumen residue and high solid contents are transported to the tailing ponds.¹³ However, the bitumen residue has become a threat to wildlife and the environment.^{14–16} Consequently, it is crucial to separate bitumen from tailings before disposing of them in tailings ponds. The first step to designing a separation technology is understanding the tailings flow and its effective parameters. However, the low bitumen concentration in the slurry and the complexity of the mixture make separation difficult. It is difficult to predict the transport characteristics of slurry flow in large-diameter pipes, especially

when there are multiple secondary phase solids and bitumen droplets in the slurry.

A few experimental works reported a similarly complex multiphase flow system with a gas–liquid–solid flow in a horizontal pipeline. Gillies *et al.*¹⁷ experimentally investigated gas–liquid mixtures transport sand in a horizontal pipe in both laminar and turbulent flow regimes. Gas was injected into the loop, and static pressure was measured near the weighed section. They found that the gas injection would increase the solid's transport rate when the flow was turbulent and the axial pressure gradient increased. Scott and Rao¹⁸ also investigated the experimental study on the transport of solid particles (500 and 100 μm) by gas–liquid mixtures in horizontal pipes. Experimental observations were reported for different solid concentrations and pipe diameters on the saltation velocity for liquid–solid, bubble, plug, and slug flow regimes. They found that for the larger particles, the effects of bubbles and plugs on the velocity field were insufficient to overcome the forces causing saltation, and there was no significant change in actual saltation velocity.

Fukuda and Shoji¹⁹ also studied the pressure drop of an air–water–sand three-phase system in horizontal pipes. Two different flow patterns were observed, i.e., plug and slug flow. They found that pressure drop increased in proportion to the gas velocity. At a constant gas velocity, the differences in pressure drop were due to changes in the volumetric particle counteraction. Recently, Zahid *et al.*²⁰ experimentally studied the two-phase and three-phase flow behavior in drilling annuli using a high-speed visualization technique. Experimentally, they found that the air–water two-phase flow and gas bubbles were separated by water and the top of the annulus. A bubbly flow regime was observed for the considered range of operating conditions. However, with an increase in the water and air flow rate, the system pressure was increased. For lower flow rates of air and water, a stratified flow regime was observed with a clear wavy interface on the upper part of the annulus. Kaushal *et al.*²¹ experimentally investigated the pressure drop and particle concentration distribution with different combinations of particle size distributions (PSDs) and concentrations. They reported that the particle concentration in the horizontal panel was not correlated with the velocity and overall concentration. However, a lower pressure drop was obtained with a broad-grading particle and a lower velocity.

To recover residual bitumen before discharging to the tailing ponds, several innovative experimental studies have been conducted to enhance bitumen recovery with microbubble injection in a lab-scale pipeline.^{22–25} Though a vast number of theoretical and experimental studies on liquid–solid flow can be found in the literature, very few studies related to the gas–liquid–solid flow were available, and uncertainties exist in modeling this flow. Recently Motamed Dashliborun *et al.*²³ reported experimental work that the optimal bitumen recovery of 50% was achieved from the oil sand tailings of 6.68 wt. % sands and 0.2 wt. % bitumen with microbubble injection in a hydrotransport pipeline.²³ Furthermore, a higher bitumen recovery of 70% from highly concentrated oil sand tailings of 50 wt. % sands was obtained in the following work conducted by Zhou *et al.*²⁴ Numerous investigations have studied the mechanism of flotation behavior in the presence of microbubbles.^{26–28} The interaction between microbubbles and bitumen droplets decreases the system's free energy.²⁹ Due to the longer residence time and high surface-to-volume ratio, microbubbles have a higher probability of collision with bitumen droplets.^{26,30} In addition,

microbubbles have faster liquid drainage in the attachment to the bitumen surface.^{31,32} Those factors account for enhanced bitumen recovery with microbubble injection. Nevertheless, using experimental techniques, it is challenging to non-intrusively monitor the bitumen–bubble interaction in the turbulent concentrated slurry flow at a high flow rate.

Simultaneously with the effort to improve experimental results and analytical models, computational fluid dynamics (CFD) is becoming more comprehensive in investigating slurry flows in pipelines. There have been two different approaches to modeling multiphase flows: Eulerian–Eulerian (E–E) and Eulerian–Lagrangian (E–L).^{33,34} Kaushal *et al.*³⁵ studied the mixture and Eulerian two-fluid model (TFM) to simulate the transport of slurry flow of fine particles up to 50% by volume in the pipeline. The Eulerian model contributes a better prediction in both pressure drop and concentration profiles at various overall concentrations and flows velocities compared to the failure of the mixture model in predicting pressure drop with regard to the slurry concentration. Li *et al.*³⁶ numerically simulated the transport of multi-sized slurry through a pipeline employing a steady 3D hydrodynamic model based on the kinetic theory of granular flow (KTGF) model. They predict the distributions of velocity and concentration with different particle concentration and sizes, pipe diameter, and slurry velocity.

Recent works of Li *et al.*³⁷ and Zhang *et al.*³⁸ established the Eulerian multiphase flow model to investigate the effect of particle size of single and multi-sized slurry flows on transport properties under the same conditions, such as flow velocity, wall shear stress, and granular pressure distributions. The presence of fine particles is found to reduce energy consumption by changing the coarse particle's flow regime. Shi *et al.*³⁹ carried out simulations on multi-sized slurry flows in the horizontal pipeline under various swirling motions utilizing the Eulerian–Eulerian multiphase model in conjunction with the $k-\omega$ shear stress transport (SST) scheme. The results suggest that an increased level of swirl results in a higher degree of homogeneity of slurry flows.

In general, the mixture model is a low computational effort model than the E–E simulation. Our previous work systematically studied the complex multiphase flow system with eight solid phases, bitumen droplets, and carrier non-Newtonian liquid. However, the mixture model completely ignores the secondary phase interactions.⁴⁰ The equations for the mixture model are relatively similar to those for a single-phase flow but are expressed in terms of the density and velocity of the mixture. As a result, the secondary phase interactions of bubbles and bitumen droplets are neglected in our previous work due to limitations of the mixture model for high-density ratios.^{40,41} Ling *et al.*⁴² also reported that for lower flow rates and higher particle concentrations, the mixture model underpredicts the pressure drop.

Interestingly, most of the reported research is mainly concerned with the slurry transport for the lab-scale data for Newtonian liquids,^{35–39,43} while several industrial slurry systems likely exhibit complex non-Newtonian behaviors.^{44–46} On the other hand, secondary phases like droplets and bubbles play a significant role in industrial scales pipeline transport such as oil sand tailings and mining residuals.^{47–49} In spite of industrial application, most research works completely ignore the fundamental understanding of the droplets and bubble influence in a complex multiphase system phase. The underlying phenomena of droplets and bubbles in a tailing system are imperative and desirable. To the best of our knowledge, there is no published

data on slurry systems with droplets and bubbles in the literature that can provide the necessary concentration profiles and pressure drop for industrial applications. Therefore, the main objective of this study is to investigate the effect of the secondary phase interactions on the tailing transport in highly non-Newtonian turbulent flows. The present work would provide an improved design of oil sand tailing pipeline systems, where secondary phases such as droplets and bubbles are commonly presented.

In this work, we develop a three-dimensional finite volume method (FVM) based on an Eulerian–Eulerian CFD model coupled with the KTGF model to investigate the influence of secondary phase droplets and bubbles in an industrial-scale horizontal pipeline tailing system. We systematically conduct the model sensitivity analysis and model validation with the industrial scale field data. The validated CFD model is extended to investigate the bitumen droplet, bubble size, and secondary phase fraction effect on flow characteristics. These fundamental understandings can be significantly beneficial for industrial-scale slurry transport systems. This paper is organized as follows: Sec. II presents the velocity profile and pressure drop of the tailing system; Sec. III describes the governing equations of the multi-fluid model (MFM), turbulence model, and non-Newtonian viscosity model; and Sec. IV describe the details of our numerical methodology settings and model validation. In Sec. V, we present and discuss the effects of the secondary phase droplet/bubble size and fraction on slurry flow behavior. In Sec. VI, we conclude our study with some concluding remarks.

II. VELOCITY PROFILE AND PRESSURE DROP OF TAILINGS SYSTEM

Figure 1(a) shows a schematic of the horizontal pipeline used for field data (i.e., pilot scale hydrotransport pipeline data) collection. The pipe is 220 m in length and 74 cm in diameter, with two pumps at the inlet and outlet of the pipe. Several sets of field data were collected on a section of an industrial pipeline for a mining process to validate the CFD model. The samples are collected from the pipe center after the first pump discharge every 12 h, and the mixture composition is

determined using a Dean–Stark apparatus⁵⁰ to determine the particle size distribution (PSD) for solid particles sieving method employed.⁵¹

A noninvasive SANDtrac velocity profile system (CiDRA) is installed after 200 m of the pipe inlet and reports the mixture velocity distribution in five locations across the pipe every 2 s. It consists of five sensors attached to the wall of a pipe that track turbulent eddies that cause pressure disturbances and force on the wall. This array senses the dynamic strains applied to the pipe by these forces and converts them to electrical signals to be interpreted, and the velocity values are calculated.⁵²

The signals from the profiler are interpreted to the mixture velocity values in different locations. Figure 1(b) shows the measurement points of the velocity in a cross-sectional view. The device measures the mixture velocities in five locations with a 45° difference in angle. The radial distance from the pipe center is approximately 0.85R, where R is the pipe radius. The pressure is measured at two locations; at the first pump discharge and the second pump suction every 2 s. The flow rate and mixture density data are also available within a 2 s time span. The available data will be used to prepare simulation cases for model validation. Figure 1(c) shows the schematic of the oil sands tailings flow inside the pipe with its components.

The selection of a proper time window must be carefully considered after collecting around a million data points and monitoring the fluctuations and significant shifts in flow conditions. Data points are plotted against a 30-min time window as the initial step. For CFD simulations, a time window is chosen if the oscillations are insignificant and the flow conditions are fairly consistent minimum standard deviation is lower than 0.2. After averaging the values over a selected time window, simulation cases are prepared for multiple time windows listed in Table I. The particle sizes S1 and S2 represent solid 1 and solid 2 volume fractions of the tailing system.

III. MATHEMATICAL MODELING

A. Governing equations of multi-fluid model

Multiphase systems are modeled mathematically as interpenetrating continua in the Eulerian model.⁵³ The phases are considered distinct and treated in the system. The interphase exchange coefficient and pressure are responsible for phase coupling. Dissipation of energy, exchange of energy among particles, and interfacial forces are all considered in the model.^{36,43}

Table II lists the governing equation of the mass and momentum balance for the phases. The nomenclature section includes the list of all symbols mentioned in governing equations. Equation (1) shows the

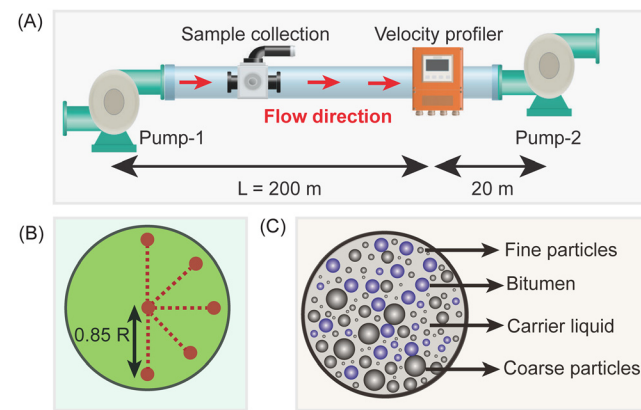


FIG. 1. Schematic representation of (a) tailing hydrotransport pipeline with dimensions, (b) velocity profiler measurement locations, and (c) typical tailing slurry representation. The tailing composition consists of coarse and fine particles with bitumen in a carrier fluid.

TABLE I. Field data of the tailing system used in the CFD model validation.

Case	V (m/s)	Solid fraction	Carrier density (kg/m ³)	Bitumen fraction	S1 (75 μm)	S2 (700 μm)
A	5.620	0.238	1335	0.0025	0.206	0.033
B	5.353	0.230	1279	0.0033	0.199	0.031
C	5.430	0.237	1329	0.0029	0.211	0.025
D	5.540	0.269	1228	0.0030	0.240	0.028
E	5.764	0.223	1223	0.0029	0.192	0.030
F	5.643	0.238	1332	0.0030	0.205	0.032

TABLE II. Momentum equations.^{40,53,54}

Continuity	$\frac{\partial}{\partial t}(\rho_q \alpha_q) + \nabla \cdot (\rho_q \alpha_q \vec{v}_q) = 0, \quad (q = l, s, b)$	(1a)
	$\alpha_l + \alpha_{s_1} + \alpha_{s_2} + \alpha_b = 1$	(1b)
Momentum (liquid)	$\frac{\partial}{\partial t}(\alpha_l \rho_l \vec{v}_l) + \nabla \cdot (\alpha_l \rho_l \vec{v}_l \otimes \vec{v}_l) = -\alpha_l \nabla p + \rho_l \alpha_l \vec{g} + \nabla \cdot \tau_l + \vec{F}_{1,s} + \vec{F}_{1,b}$	(2a)
	$\vec{F}_{1,s_i} = \vec{F}_{td,ls_i} + \vec{F}_{drag,ls_i}$	(2b)
	$\vec{F}_{drag,ls_i} = \frac{3}{4} C_D \alpha_{si} \rho_l \frac{\ \vec{v}_l - \vec{v}_{si}\ }{d_p} (\vec{v}_l - \vec{v}_{si})$	(2c)
	$\vec{F}_{td,ls_i} = \frac{3}{4} \frac{C_D \mu_{t,l}}{d_p \sigma_{t,l}} \alpha_{si} \ \vec{v}_l - \vec{v}_{si}\ \left(\frac{\nabla \alpha_{si}}{\alpha_{si}} - \frac{\nabla \alpha_l}{\alpha_l} \right)$	(2d)
	$\vec{F}_{1,b} = \vec{F}_{td,lb} + \vec{F}_{drag,lb}$	(2e)
	$\vec{F}_{drag,lb} = \frac{3}{4} C_D \alpha_b \rho_l \frac{\ \vec{v}_l - \vec{v}_b\ }{d_b} (\vec{v}_l - \vec{v}_b)$	(2f)
	$\vec{F}_{td,lb} = \frac{3}{4} \frac{C_D \mu_{t,l}}{d_p \sigma_{t,l}} \alpha_b \ \vec{v}_l - \vec{v}_b\ \left(\frac{\nabla \alpha_b}{\alpha_b} - \frac{\nabla \alpha_l}{\alpha_l} \right)$	(2g)
Momentum (<i>i</i> th solid phase)	$\frac{\partial}{\partial t}(\alpha_{si} \rho_{si} \vec{v}_{si}) + \nabla \cdot (\alpha_{si} \rho_{si} \vec{v}_{si} \otimes \vec{v}_{si}) = -\alpha_{si} \nabla p - \nabla p_{si} + \rho_l \alpha_{si} \vec{g} + \nabla \cdot \tau_{si} + \vec{F}_{si,l} + \vec{F}_{drag,si,b} + \beta_{ij}(\vec{v}_{sj} - \vec{v}_{si})$	(3a)
	$\beta_{ij} = \frac{3(1 + e_{ij}) \left(\frac{\pi}{2} + C_{fr,ij} \frac{\pi^2}{8} \right) \alpha_{si} \rho_{si} \alpha_{sj} \rho_{sj} (d_{si} + d_{sj})^2 g_{0,ij}}{2\pi(\rho_{si} d_{si}^3 + \rho_{sj} d_{sj}^3)} \ \vec{v}_{si} - \vec{v}_{sj}\ $	(3b)
	$\tau_{si} = \alpha_{si} \mu_{si} (\nabla \vec{v}_{si} + (\nabla \vec{v}_{si})^T) + \alpha_{si} \left(\lambda_{si} - \frac{2}{3} \mu_{si} \right) (\nabla \cdot \vec{v}_{si}) \vec{I}$	(3c)
	$\vec{F}_{drag,s} = -\vec{F}_{drag,l}$	(3d)
	$\vec{F}_{td,s} = -\vec{F}_{td,l}$	(3e)
Momentum (bitumen)	$\frac{\partial}{\partial t}(\alpha_b \rho_b \vec{v}_b) + \nabla \cdot (\alpha_b \rho_b \vec{v}_b \otimes \vec{v}_b) = -\alpha_b \nabla p + \rho_l \alpha_b \vec{g} + \nabla \cdot \mu_b (\nabla \vec{v} + \nabla \vec{v}^T) + \vec{F}_{b,l} + \vec{F}_{b,si}$	(4a)
	$\vec{F}_{b,l} = -\vec{F}_{1,b}; \vec{F}_{b,si} = -\vec{F}_{si,b}$	(4b)

continuity equation for all of the phases. Equation shows the momentum balance for the liquid (carrier fluid), which is the primary phase in this study. In this equation, $\vec{F}_{1,s}$ and $\vec{F}_{1,b}$ refer to the interphase forces between the liquid with the solids and bitumen phases, respectively. For the interactions between the liquid and solid phases, the drag force [Eq. 2(c)], virtual mass [Eq. 2(d)], and turbulent dispersion force [Eq. 2(e)] are included in the model. The drag force arises from the difference between the velocities of the primary and secondary phases in the flow direction. The drag force has been proven to be an essential force in the modeling of multiphase slurry flows. The drag model of Gidaspow *et al.*⁵⁶ has been extensively used by other researchers in the literature and proven to accurately describe the drag force between the solid and liquid phase.^{36,43,53} In a turbulent slurry flow, the interactions between the turbulent eddies and secondary phases resulting in the turbulent dispersion force can significantly influence the flow behavior and should be included in the model.^{57–59} To this end, the model introduced by Burns *et al.*⁵⁷ is implemented to account for the turbulent dispersion force between the carrier and solid particles.

For the interactions between the carrier fluid and bitumen droplets, the drag [Eq. 2(f)] and turbulent dispersion [Eq. 2(g)] forces have been included in the model similar to carrier–solids interactions. The drag model used for the carrier–bitumen is the symmetric model,⁴⁰ and the model of Burns *et al.*⁵⁷ has been implemented for the turbulent dispersion force. The drag force of Gidaspow *et al.*⁵⁶ has been included to capture the interphase force between the solid phases. For the bitumen and solid phases, the symmetric drag model has been used.

B. Governing equations of turbulence model

The $k-\epsilon$ and $k-\omega$ are the most promising turbulence models, and numerous studies have reported their applicability and implementation in the slurry system. However, several researchers recently reported the feasibility of the standard $k-\epsilon$ model for complex slurry systems.^{36,60} Considering the computational cost for industrial-scale systems with four and five phases of the E–E model, the two-equation

TABLE III. Standard $k-\epsilon$ mixture turbulence model.³⁶

The k equation	$\frac{\partial}{\partial t}(\rho_m k) + \nabla \cdot (\rho_m \vec{v}_m k) = \nabla \cdot \left(\frac{\mu_{t,m}}{\sigma_k} \nabla k \right) + G_{k,m} - \rho_m \epsilon$	(5a)
The ϵ equation	$\frac{\partial}{\partial t}(\rho_m \epsilon) + \nabla \cdot (\rho_m \vec{v}_m \epsilon) = \nabla \cdot \left(\frac{\mu_{t,m}}{\sigma_\epsilon} \nabla \epsilon \right) + \frac{\epsilon}{k} (C_{1\epsilon} G_{k,m} - C_{2\epsilon} \rho_m \epsilon)$	(6a)
Mixture density	$\rho_m = \sum_{q=1}^n \alpha_q \rho_q$	(7a)
Mixture velocity	$\vec{v}_m = \left(\sum_{q=1}^n \alpha_q \rho_q \vec{v}_q \right) / \left(\sum_{q=1}^n \alpha_q \rho_q \right)$	(8a)
Turbulent viscosity	$\mu_{t,m} = \rho_m C_\mu \frac{k^2}{\epsilon}$	(9a)
Standard constants	$C_{1\epsilon} = 1.44, C_{2\epsilon} = 1.92, C_\mu = 0.09, \sigma_k = 1.0, \sigma_\epsilon = 1.3$	(10a)

model is taken into account. The choice of the turbulence model between these two models has been widely discussed in the literature for different engineering applications. Inspired by the previous works, a mixture turbulence $k-\epsilon$ model based on Reynolds-averaged Navier–Stokes (RANS) equations is used to capture the turbulent slurry flow.^{36,60} The $k-\epsilon$ model equations describing this model are listed in Table III. The standard wall functions based on the Launder–Spalding law-of-the-wall is the most widely used wall function.^{61,62} The standard wall functions provide reasonably accurate predictions for most of the high-Reynolds number, wall-bounded flows. This model has been extensively used in similar systems like horizontal pipes without elbow junctions, and strong body forces systems.^{63–67} The Y^+ value near the wall is between $30 < Y^+ < 300$ for both carrier and secondary phase solids. The logarithmic law for mean velocity is valid in the present study. The standard wall functions-based model has a faster and easier convergence than SST $k-\omega$, and the near-wall effect is insignificant. Therefore, we have adopted the Standard Wall Functions treatment similar to previous works.

C. Casson viscosity model

According to Adeyinka *et al.*,⁶⁸ the suspension of fine sand particles in water with a concentration in the range of 10–40 wt. % follows the Casson rheological model. As the mass fraction of the fine particles in this study fall into the mentioned range, the non-Newtonian behavior of the carrier model can be modeled via the Casson model. The equation for this model is expressed via Eq. (11), where μ_c is the Casson viscosity,

$$\tau^{1/2} = \tau_y^{1/2} + \mu_c^{1/2} \dot{\gamma}^{1/2}. \tag{11}$$

IV. IMPLEMENTATION AND VALIDATION OF CFD MODELS

A. Computational model and solver settings

In this work, a three-dimensional circular pipeline with the inner diameter of $D = 0.74$ m and length of $Z = 105$ m is considered for the numerical investigation based on the industrial scale pipeline conditions as shown in Fig. 2(a). Based on the computed velocity profiles along the slurry pipeline, it is confirmed that the flow is fully

developed. This study employs an unsteady state Eulerian–Eulerian multiphase model in which different phases are conceptualized as interpenetrating continuous systems. To describe particle interactions, granular kinetic theory is used. All phases share a single pressure, and each phase solves its corresponding conservation equations for mass, momentum, and energy. All phases are coupled by pressure and

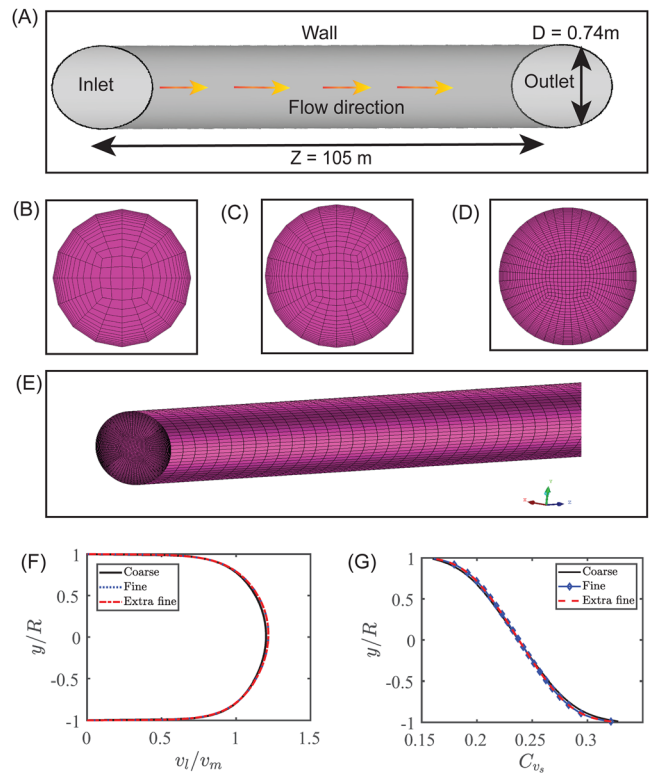


FIG. 2. (a) Computational domain with dimensions and boundary conditions. Cross-sectional view of the mesh for different mesh structures: (b) coarse, (c) fine, (d) extra fine, and (e) grid structure along the length of the pipeline. Comparison of (f) velocity profile and (g) solid volume fraction profiles for different meshes.

05 March 2024 21:31:26

TABLE IV. Equations from granular kinetic theory.^{36,53–55}

Granular kinetic theory (ith solid phase)	$\lambda_{s_i} = \frac{4}{3} \alpha_{s_i}^2 \rho_{s_i} d_{s_i} g_{0,ii} (1 + e_{ij}) \left(\frac{\Theta_{s_i}}{\pi} \right)^{1/2} \quad (12a)$
	$g_{0,ii} = \left[1 - \left(\sum_{i=1}^2 \alpha_{s_i} / \alpha_{s, \max} \right)^{1/3} \right]^{-1} + \frac{d_{s_i}}{2} \sum_{i=1}^2 \frac{\alpha_{s_i}}{d_{s_i}} \quad (12b)$
	$g_{0,ij} = \frac{d_{s_i} g_{0,ii} + d_{s_j} g_{0,ij}}{d_{s_i} + d_{s_j}} \quad (12c)$
	$\Theta_{s_i} = \frac{1}{3} \bar{v}'_{s_i} ^2 \quad (12d)$
	$0 = \left(-p_{s_i} \bar{I} + \bar{\tau}_{s_i} \right) : \nabla \bar{v}_{s_i} - \gamma_{\Theta_{s_i}} + \phi_{li} \quad (12e)$
	$\gamma_{\Theta_{s_i}} = \frac{12(1 - e_{ij}^2) g_{0,ii}}{d_{s_i} \pi^{1/2}} \rho_{s_i} \alpha_{s_i}^2 \Theta_{s_i}^{3/2} \quad (12f)$
	$\phi_{li} = -3K_{li} \Theta_{s_i} \quad (12g)$
	$p_{s_i} = \alpha_{s_i} \rho_{s_i} \Theta_{s_i} \left[1 + 2 \sum_{j=1}^2 \left(\frac{d_{s_i} + d_{s_j}}{2d_{s_i}} \right)^3 (1 + e_{ij}) \alpha_{s_j} g_{0,ij} \right] \quad (12h)$
	$\mu_{s_i} = \mu_{s_i, \text{col}} + \mu_{s_i, \text{kin}} + \mu_{s_i, \text{fr}} \quad (12i)$
	$\mu_{s_i, \text{col}} = \frac{4}{5} \alpha_{s_i} \rho_{s_i} d_{s_i} g_{0,ii} (1 + e_{ij}) \left(\frac{\Theta_{s_i}}{\pi} \right)^{1/2} \alpha_{s_i} \quad (12j)$
	$\mu_{s_i, \text{kin}} = \frac{10 \rho_{s_i} d_{s_i} (\Theta_{s_i} \pi)^{1/2}}{96 \alpha_{s_i} (1 + e_{ij}) g_{0,ii}} \left[1 + \frac{4}{5} g_{0,ii} \alpha_{s_i} (1 + e_{ij}) \right]^2 \alpha_{s_i} \quad (12k)$
	$\mu_{s_i, \text{fr}} = \frac{p_{s_i} \sin \varphi_{s_i}}{2I_{2D}^{1/2}} \quad (12l)$

interphase exchange coefficients. In this method, volume fractions of continuous and dispersed phases are assumed to be continuous functions of space and time, and their sum is equal to one. Also, interphase exchange coefficients are used to model all secondary phase interactions. For secondary phase interactions, the E–E model is more comprehensive and robust from a computational perspective. The current study uses the E–E multi-fluid model (MFM). It is worth noting that in the present CFD model, droplet/bubble breakup and coalescence are not considered.

Tables II and IV list the conservation equation for the multi-fluid model with KTGF. A finite volume method (FVM) based commercial software ANSYS Fluent solver 2020 R2 is used to solve all unsteady state equations.⁴⁰ The details of the solver settings and schemes are presented in Table V. At the pipe inlet, each phase’s velocity and volume concentration is assumed to be uniform. An outlet boundary condition equal to atmospheric pressure is selected as the outlet boundary condition. At the wall, the liquid phase velocity is set to zero, corresponding to the no-slip condition. Turbulence intensity and turbulent viscosity ratio of all phases are set to the values 5% and 10%, respectively.³⁶

The details of all the fluid properties and KTGF model parameters are listed in Table VI. For solving momentum equation and

TABLE V. List of different models and solver settings details of the multi-fluid model.

Model	Scheme
Multiphase model	Eulerian
Turbulence model	<i>k</i> – <i>ε</i> standard ³⁶
Turbulent dispersion	Burns <i>et al.</i> ⁵⁷
Turbulence multiphase	Mixture ⁵³
Carrier–solid drag	Gidaspow ^{53,56}
Carrier–bitumen drag	Symmetric ^{40,69}
Solid–bitumen drag	Symmetric ^{40,69}
Solid–solid drag	Gidaspow ^{53,56}
Pressure–velocity coupling	Phase coupled SIMPLE
Pressure	PRESTO
Momentum	Second order upwind
Volume fraction	First order upwind
Turbulent kinetic energy and dissipation rate	Second order upwind
Transient formulation	Second order implicit
Carrier fluid shear condition	No-slip
Bitumen shear condition	No-slip
Carrier viscosity	Casson viscosity model ⁶⁸
Time step	0.01 s
Number of time steps	20 000

turbulence transports, the second-order upwind method is used. For solving volume fraction, the first-order upwind method is used with a pressure relaxation factor of 0.3, a momentum relaxation factor of 0.7, and a volume fraction relaxation factor of 0.4. The governing equations must be discretized in space and time for transient simulations. Time-dependent equations are discretized spatially in the same way as steady-state equations. In temporal discretization, each differential equation term is integrated over the time step δt . The implicit equation can be solved iteratively at each time level. The advantage of the implicit scheme is that it is unconditionally stable with respect to time

TABLE VI. Material parameters and boundary conditions used in CFD simulations.

Parameter	value
Pipe diameter (m)	0.74
Pipe length (m)	105
Particle diameter (μm)	75 and 700
Density of the particle (kg/m^3)	2650
Carrier density (kg/m^3)	1335
Bitumen viscosity (Pa s)	20
Casson viscosity μ_c ($\text{Pa}^{1/2} \text{s}^{1/2}$)	0.0035 (Ref. 68)
Yield stress, τ_y (Pa)	0.0016 (Ref. 68)
Fraction packing limit	0.60 (Ref. 40)
Angle of internal friction	30 (Ref. 40)
Particle–particle restitution coefficient	0.90 (Refs. 36 and 70)
Particle–wall specular coefficient	0.20 (Ref. 71)

step size. Therefore, the transient formulation is discretized using the second-order implicit scheme.

In the present study, density, body forces, granular temperature, turbulent kinetic energy, turbulent dissipation rate, and turbulent viscosity relaxation factors are concurrently maintained at their default values of 1, 1, 0.2, 0.8, 0.8, and 1, respectively. The relative error between two successive iterations was specified by using a convergence criterion of 10^{-4} for each scaled residual component. The residual components are continuity and momentum components for the carrier liquid, solid-1, solid-2, bitumen, and bubble. In addition to continuity and momentum, k , epsilon, and volume fraction of solid-1, solid-2, bitumen, and bubbles, the gravitational acceleration $g = -9.8 \text{ m}^2/\text{s}$ is considered in the Y -direction. Time step sensitivity is also investigated from 0.0001 s to 0.01 by comparing the velocity profiles, and there is no change in the results. Therefore, for all the cases, a fixed time step 0.01 s is considered for this study.

All the simulations are performed in the high-performance computing (HPC) facility at Compute Canada Ceder cluster with 44 CPUs, and the simulations are solved for 20000-time steps for the period of 200 s flow time. After reaching 100 s most of the simulation reached a steady state. However, all simulations are run for 200 s to obtain accurate and reliable data. A relatively long period of time that ensures the flow has reached a steady state. All the results are analyzed at $Z = 90 \text{ m}$ by drawing a cross-sectional YX plane and distribution profiles are analyzed, creating a vertical reference line middle of the YX plane.

B. Grid independence study

The first grid independence study is conducted to understand the mesh density on flow characteristics, as depicted in Figs. 2(b)–2(d). Three different meshes, such as, coarse, fine, and extra fine meshes,

are examined to ensure good quality computations and convergence of the models. The number of nodes for coarse, fine, and extra fine meshes are 1 68 682, 3 39 500, and 5 27 253, respectively. To ensure the accuracy of a computational model, the average mesh quality is verified based on the skewness from 0.72 to 0.94 for three meshes. To capture the near-the-wall effect, 30 boundary layers are considered. The 3D computational structured mesh is portrayed in Fig. 2(e). The velocity profiles along the vertical reference line are analyzed at $Z = 100 \text{ m}$ for all the cases. Figures 2(f) and 2(g) results demonstrated that fine and extra fine mesh results are almost identical for velocity profile and solids concentration profiles. Therefore, the fine grid and the number of nodes are sufficient to capture the flow physics accurately. The y^+ values are also monitored for the fine grid, the maximum y^+ for the second phase is 0.063, and for the mixture phase 4.27, which clearly shows that the grid is fine enough near the wall.

C. Drag models and particle size sensitivity analysis

The momentum exchange between the two dispersed phases, viz., droplets and solid phases, have to be taken into account for CFD simulation of three-phase and four-phase flows since the droplets/bubbles tend to follow in the slurry system like a fluid phase. The selection of appropriate drag models is also essential for multiphase modeling.⁶⁰ To study the sensitivity of drag models between carrier-bitumen and solid-bitumen, drag models are carefully studied. In the open literature, different drag models are available such as Schiller–Naumann,⁷² Morsi–Alexander,⁷³ Symmetric,⁴⁰ Grace *et al.*,⁷⁴ Takamasa and Tomiyama,⁷⁵ and Ishii.⁷⁶

Figure 3(a) demonstrates the velocity profile data comparison with field data for different carrier-bitumen drag models. It is interesting to note that all the selected drag models showed similar trends with the field data. In contrast, symmetric drag models showed better prediction than other models, with a maximum deviation of 2.71% in

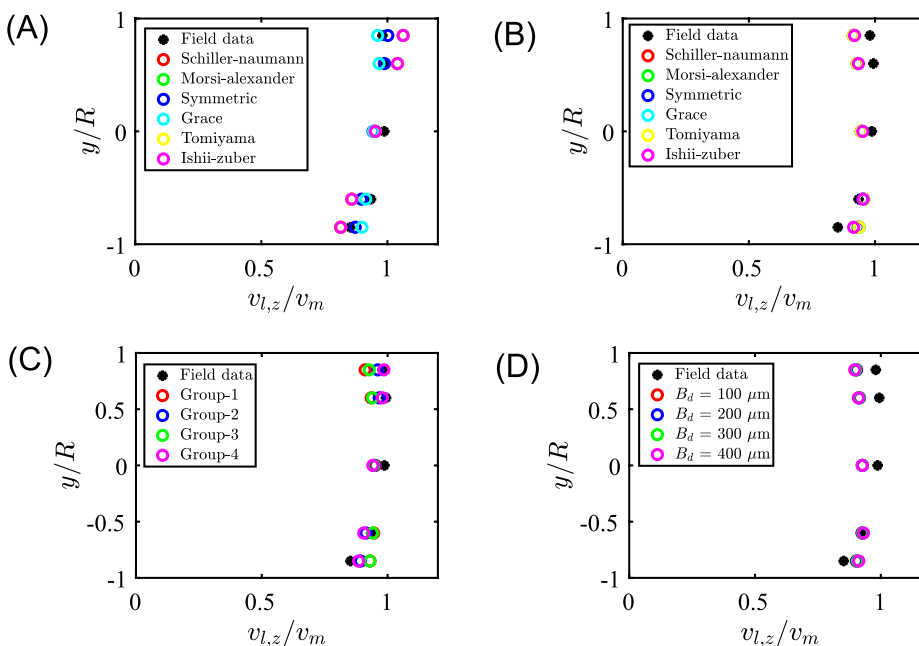


FIG. 3. Comparison of a velocity profile for different (a) carrier-bitumen drag models, (b) solid-bitumen drag models, and (c) combination of particle sizes. Group-1: 200 and 500 μm , Group-2: 200 and 700 μm , Group-3: 75 and 500 μm , and Group-4: 75 and 700 μm . (d) Bitumen droplet size. All the properties are considered for case-A, from Table I.

terms of average velocity deviation. There is a distinct difference between the drag model predictions at the bottom and the top of the pipe. Notably, the average velocity deviation is two times greater than the symmetric drag model.

Since the two dispersed phases are assumed to be continua in our system, it is necessary to model the drag force between the solid particles and droplets/bubbles in the same way as the primary–secondary phases. The drag model between the solid–bitumen (i.e., drag models between secondary phases) is comprehensively studied as shown in Fig. 3(b). Even though all the drag models showed similar agreement with the field data, the results are further analyzed based on the pressure drop and compared with field data as listed in Table VII. The symmetric drag model exhibited trustworthy prediction in terms of velocity profile agreement and pressure drop. Therefore, the symmetric drag model is considered between the carrier–bitumen and solid–bitumen in this study. The most popular Gidaspow *et al.*⁵⁶ drag model is used between the carrier–solid and solid–solid phase. A recent study of Sadeghi *et al.*⁵³ also successfully demonstrated the applicability of Gidaspow *et al.*⁵⁶ drag model prediction in a slurry system.

Furthermore, the effect of particle size combination and bitumen droplet is also comprehensively investigated. Simulating the whole particle sizes is challenging due to computational time and convergence issues with E–E multifluid models. To simplify the computational model, two solid particles are considered by covering the whole range of particle sizes. Small and larger particles are considered in different combinations to cover the full PSD range. Figure 3(c) shows the velocity profile field data agreement with a range of particle size combinations. The CFD prediction revealed that group-4 in combination with smaller particle size 75 μm and coarse particle size 700 μm showed excellent agreement with field data measurements, and the corresponding pressure drop is also found to be good in agreement. The considered particle size combination with the smaller particle size of 75 μm and the coarse particle size of 700 μm represents the general oil sand tailing system. These results also indicate small and large particle combinations are more likely to describe the tailings compositions. Therefore, based on the velocity profile and pressure drop data (Table VIII comparison with the field data), group-4 particle size combination (i.e., solid 1–75 μm and solid 2–700 μm) is considered for further investigations. For simplicity, solid 1 and solid 2 are referred to as S1 and S2. The influence of bitumen droplet size is also investigated

TABLE VII. A comparison of velocity and pressure error percentages for different drag models.

Model	Average velocity error %		Pressure drop error %	
	Carrier–bitumen	Solid–bitumen	Carrier–bitumen	Solid–bitumen
Schiller–Nauman ⁷²	5.84	5.78	1.28	4.69
Moris–Alexander ⁷³	5.85	5.80	1.26	3.77
Symmetric ⁴⁰	2.71	5.62	4.86	4.20
Grace ⁷⁴	5.84	5.81	1.16	3.40
Tomiyama ⁷⁵	5.84	5.79	1.28	2.83
Ishi–Zuber ⁷⁶	5.58	5.14	1.25	9.20

TABLE VIII. A comparison of velocity and pressure error percentages for bitumen droplet and particle size combinations.

Study	Size (μm)	Average velocity error %	Pressure drop error %
Particle combination	Group-1: 200 and 500	5.36	4.86
	Group-2: 200 and 700	3.11	4.65
	Group-3: 75 and 500	4.97	1.30
	Group-4: 75 and 700	2.70	0.61
Bitumen droplet	100	5.81	1.65
	200	5.81	1.89
	300	5.80	2.24
	400	5.78	2.69

for ranges from 100 to 400 μm based on the literature data.^{77,78} Figure 3(d) revealed that trends are identical for all the considered cases. Therefore, on the basis of a comprehensive analysis of the velocity profile and pressure drop agreement with the field data, the bitumen droplet size is chosen as 400 μm in the present study. The maximum average error percentage is 5.80, which is a highly acceptable range. It is also worth noting that in the experimental measurements, the measured velocity data corresponds to the total mixture velocity. On the one hand, numerical diffusion and model assumptions are also responsible for the deviation. However, the developed E–E model displays each phase velocity rather than the mixture velocity. This is also another possible reason for the deviation with field data.

D. Model validation with field data

To demonstrate the accuracy of the developed CFD model, the model forecasts are examined with six sets of field data of velocity distribution and pressure gradient. Figures 4(a)–4(f) provides an overview of the comparison between the CFD-predicted velocity distribution and the measured ones at the field for six different sets. The comprehensive CFD model is established by carefully considering all the sensitivity investigations and model parameters discussed in Sec. IV C. The CFD model predictions are found to be in excellent accordance with the carrier fluid velocity field data. For all the cases, the maximum average velocity error is lower than 5%. The maximum error is found near the bottom wall for all the cases. This might be due to the accumulation/dynamics of coarse solid particles at the bottom wall. On the other hand, measuring the accurate field data is also challenging due to bed formation at the bottom wall. However, the CFD model agreement showed excellent agreement with other data points.

Furthermore, the adequacy of the developed multiphase CFD model and the reliability of the prediction are also analyzed by the comparison of the CFD model predicted the pressure gradient and field data from the industrial pipeline, as portrayed in Fig. 5. The CFD model prediction demonstrated exceptional agreement with field data with a maximum error lower than 10%, indicating the CFD model efficacy. The magnified view of the six data sets agreement is also displayed in Fig. 5. In summary, the developed CFD model established the accuracy of forecast with field data in terms of velocity field and pressure drop for different sets of data. As a result, the developed CFD

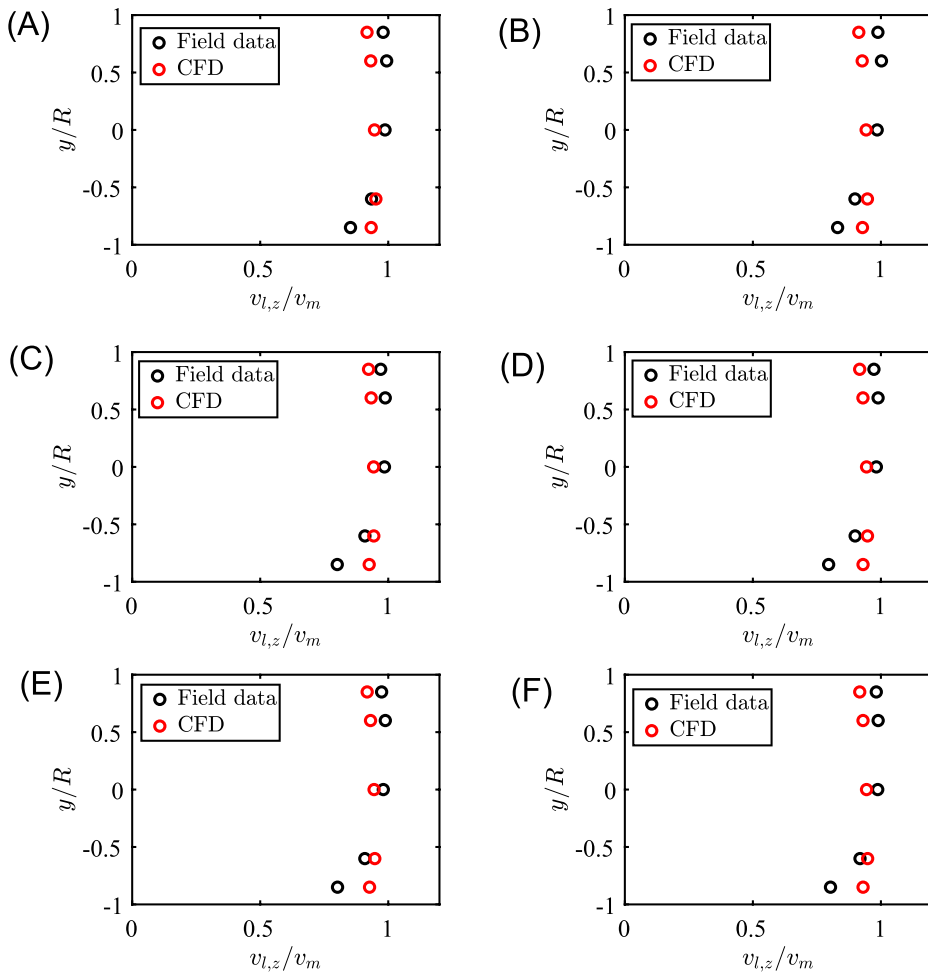


FIG. 4. Comparison of velocity distribution field data with CFD model results for different cases of (a)–(f). The red circles represent the CFD predictions, and the black color represents the field data. Detailed data on all the fluid properties and flow conditions for pressure drop validation are provided in [Table I](#).

model provides highly reliable predictions for industrial slurry systems with an acceptable error deviation.

V. PARAMETRIC STUDY

A. Effect of bitumen droplet size

In this section, the effect of bitumen droplet size in a tailing slurry system is systematically investigated. The influences of bitumen droplet

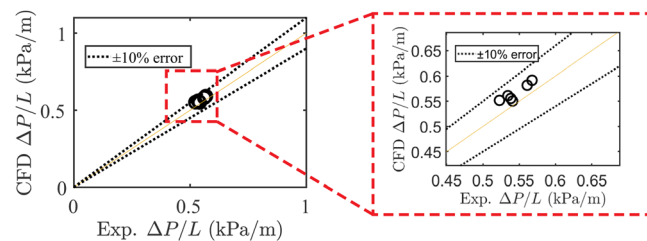


FIG. 5. Parity plot of pressure drop comparison with CFD predictions. The magnified view shows CFD vs field data points with an error of less than 10%. Detailed data on all the fluid properties and flow conditions for model validation are provided in [Table I](#).

size on solid particles distribution, velocity, solids, and bitumen profiles are studied at a fixed operating condition as reported in [Table I](#) for case A. [Figure 6](#) shows the small (i.e., solid-1), coarse (i.e., solid-2), and bitumen droplet distribution across the pipe at $Z = 100$ m.

It is evident from [Fig. 6\(a\)](#) that the solid concentration distribution is completely different for both small and coarse particles. In the case of small particles, the solid fraction is mainly distributed from the top of the pipe to the bottom part of the pipe. The coarse particles are accumulated at the bottom part of the pipe, where the small particle fraction is minimal. This is mainly due to the gravitational force acting on the large particles that leads to accumulate at the bottom part of the pipe. Gravitational forces result in particle distributions being symmetric in the horizontal direction but asymmetric vertically.

The bitumen distribution is analyzed under the same operating conditions, and it is found that bitumen droplets are mainly distributed from top to center of the pipe. This may be due to the fact that the small bitumen droplets accumulated at the top region in a highly turbulent flow similar to the small solid particles. In other words, the interaction force between the solid particles and bitumen droplets also changes bitumen droplet dynamics in a turbulent flow.

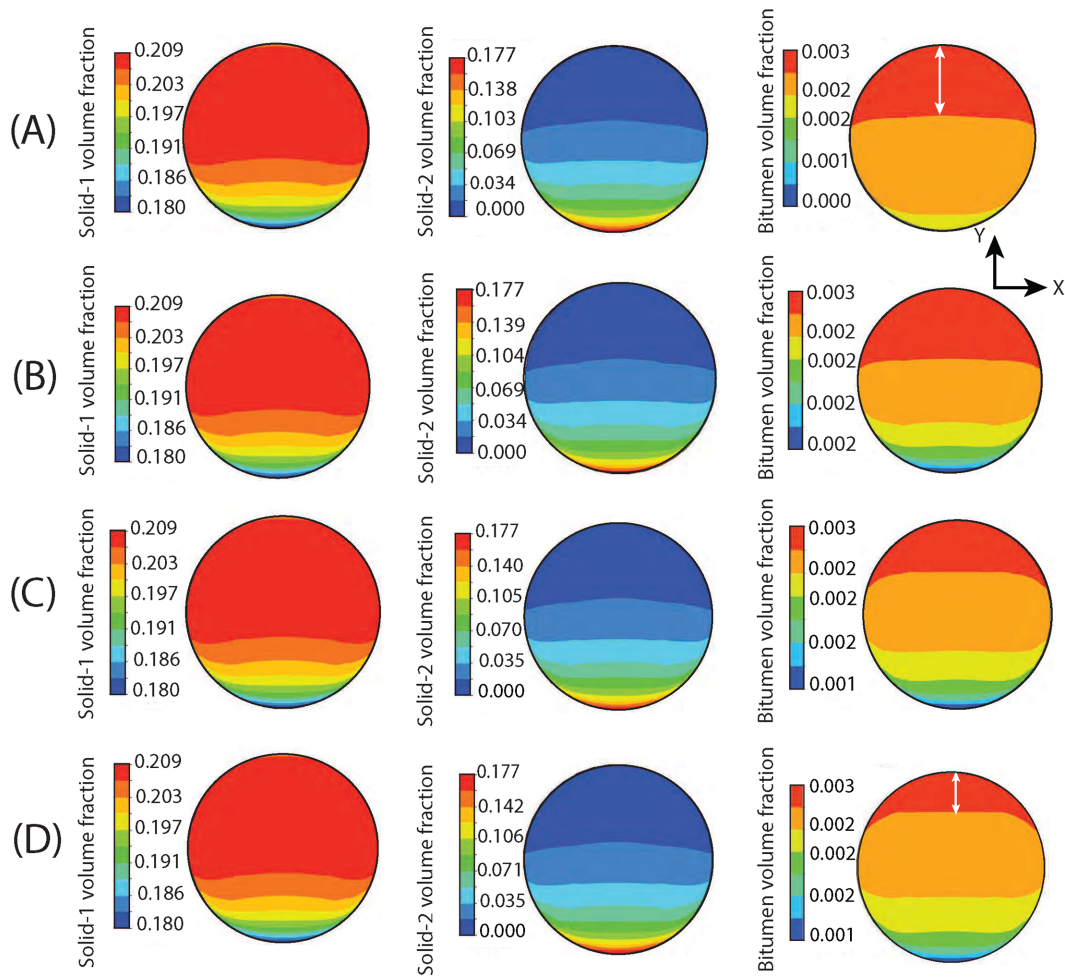


FIG. 6. The contour of solid-1, solid-2, and bitumen distribution across the pipe at $Z = 100$ m for different droplet sizes. (a) $B_d = 100 \mu\text{m}$, (b) $B_d = 200 \mu\text{m}$, (c) $B_d = 300 \mu\text{m}$, and (d) $B_d = 400 \mu\text{m}$ at a fixed bitumen fraction of 0.0025 and operation conditions.

The solid particle distribution with an increase in the bitumen droplet size from $B_d = 100$ to $400 \mu\text{m}$ is almost identical to the qualitative observation, as shown in Figs. 6(b)–6(d). For all the cases, the coarse particle concentration is relatively higher at the bottom part of the pipe. As a result, the dynamics of coarse particle motion are relatively low at the bottom due to an increase in the particle–particle and particle–wall friction in the bottom region. The degree of asymmetry in the coarse particle distribution increases with increasing bitumen droplet size because the particle–bitumen interactions are more significant, as shown in Fig. 6(d). Therefore, the velocity in the bottom region is lower than the center and top part of the pipe compared to the low solid concentration region. However, with an increase in the bitumen droplet size, the bitumen concentration accumulated in a specific smaller region at the top part of the pipe. Moreover, this observation indicated that small size bitumen droplets distributed across the pipe are similar to small solid particles. However, this phenomenon is different when bitumen droplet size increases from 100 to $400 \mu\text{m}$.

This is mainly due to the amount of bitumen fraction in the domain being the same for all the conditions. Therefore, a larger bitumen accumulation is observed at the top region in contrast to a smaller bitumen droplet observation.

To determine the influence of bitumen droplet size on the flow characteristics, such as velocity and chord-average total solid concentration, bitumen distribution profiles are analyzed at $Z = 100$ m across the pipe as shown in Figs. 7(a)–7(c). All the flow profiles are analyzed at the centerline of the pipe from the bottom to the top. Figure 7(a) indicates that the maximum velocity magnitude is observed at the center of the pipe, and velocity gradually decreases from the center of the pipe to the bottom and top with an increase in bitumen droplet size, the change in the carrier velocity profile is minimal. Numerical predicted carrier velocity profile trends also corroborated with the findings of slurry flow systems in pipelines from the study by Wang *et al.*⁷⁹ and Bordet *et al.*⁸⁰ This observation may be due to the low bitumen fraction for all the cases. The influence of bitumen droplet size on

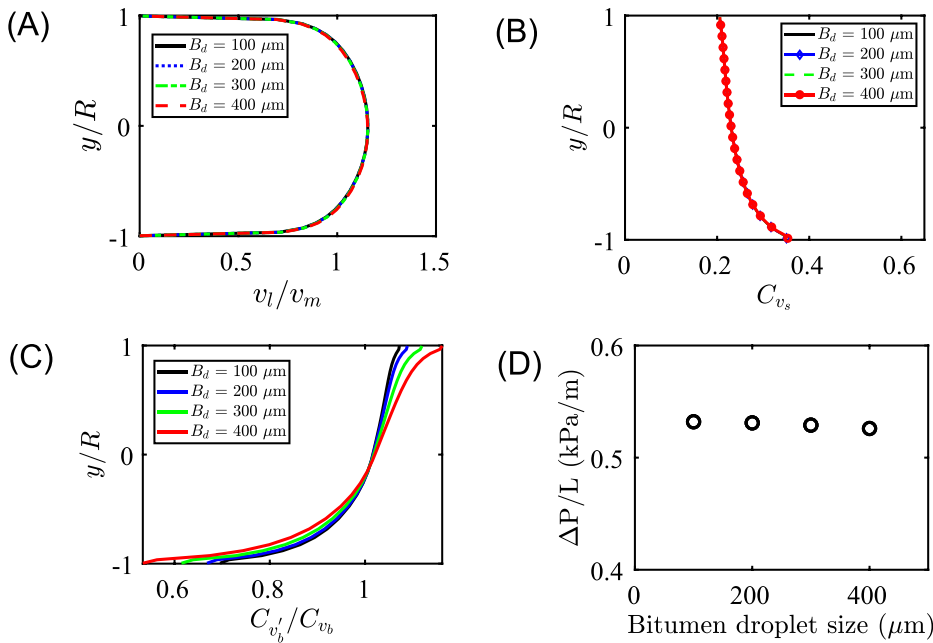


FIG. 7. Effect of bitumen droplet size on (a) velocity profiles, (b) chord-average total solid concentration profiles, (c) bitumen distribution plots, and (d) pressure drop at a fixed bitumen fraction of 0.0025 and operation conditions.

the initial bitumen concentration range may not be enough to alter the velocity profile characteristics. This suggests that the change in secondary phase droplet size has a minimal effect on the velocity profile.

Figure 7(b) represents the chord-average total solid concentration profiles for different bitumen droplet sizes. From the profiles, the effects from bitumen droplet size are negligible on the concentration profiles, as shown in Fig. 7(b). The concentration gradient near the pipe bottom is higher compared to the pipe top region. A similar observation is reported in the bimodal particles in both experimental and numerical simulations.^{21,36,37,81} This may be due to solid particle accumulation at the bottom part of the pipe, and particle momentum is relatively low compared to the center of the pipe.

Figure 7(c) depicts the bitumen distribution along a vertical line at a constant bitumen fraction in different bitumen droplet sizes. The bitumen profiles display that with an increase in the bitumen droplet size, the bitumen composition is relatively increased at the top part of the pipe. However, the bitumen fraction gradually decreases until the middle of the pipe. This implies that bitumen droplet size significantly influences the distribution of bitumen. The bitumen distribution is almost identical for all the considered ranges of bitumen droplet size at the middle of the pipe. In the case of larger bitumen droplets, the bitumen fraction considerably lowered compared to smaller droplets at the bottom of the pipe. This is because the coarse particles mainly accumulated at the bottom of the pipe, where the second phase interacts with coarse particles. This can result in smaller bitumen droplets being trapped between the particles in the bottom regime. This might be a consequence of the greater role played by particle–particle and particle–bitumen droplet interactions at the bottom part of the pipe.

Figure 7(d) shows the frictional pressure drop for different bitumen droplet sizes. Results show that increasing bitumen droplet size results in a decrease in pressure drop. However, the change pressure drop is not prominent for the considered range of bitumen droplet size and operating conditions. In the case of smaller bitumen droplets,

the interaction between secondary phases significantly contributes to a higher pressure drop due to the distribution of small particles and bitumen droplets from the top part of the pipe to the bottom part. In addition, the interaction between particle–particle also contributes to increased pressure drop.

B. Effect of bitumen fraction

To investigate the effect of bitumen fraction in tailing slurry systems, different bitumen compositions are considered from 0.0025 to 0.01, which is typically an industrial bitumen fraction range in tailing residuals. Figure 8 shows the solid particles and bitumen droplet distribution of contour plots for different bitumen fractions. The obtained numerical results reveal that for lower bitumen fraction conditions, small particles are distributed evenly from the top part of the pipe to the center of the pipe, as shown in Fig. 8(a). The concentration of fine particles gradually increases in the bottom half of the pipe, and the asymmetry of the fine particle concentration profile along the vertical direction decreases. The gravitational force acts on coarse particles, causing most particles to accumulate at the bottom of the pipe. It is evident from top to center that the coarse fraction is minimal, while bitumen droplets and small particles are distributed throughout the pipe.

An increase in the bitumen fraction showed a negligible impact on the small particle distribution across the pipe at $Z = 100\text{ m}$ as shown in Figs. 8(b)–8(d). The variation in coarse particle distributions is qualitatively similar to an increase in the bitumen fraction, but the distribution of coarse particles height from the bottom to the top part of the pipe slightly decreased as expected. In other words, the solid concentration is nearly constant in the horizontal direction, and a noticeable variation in the vertical direction is observed as the bitumen fraction increases. The results indicate that coarse particle fraction distribution increases when bitumen fraction increases. This may be due

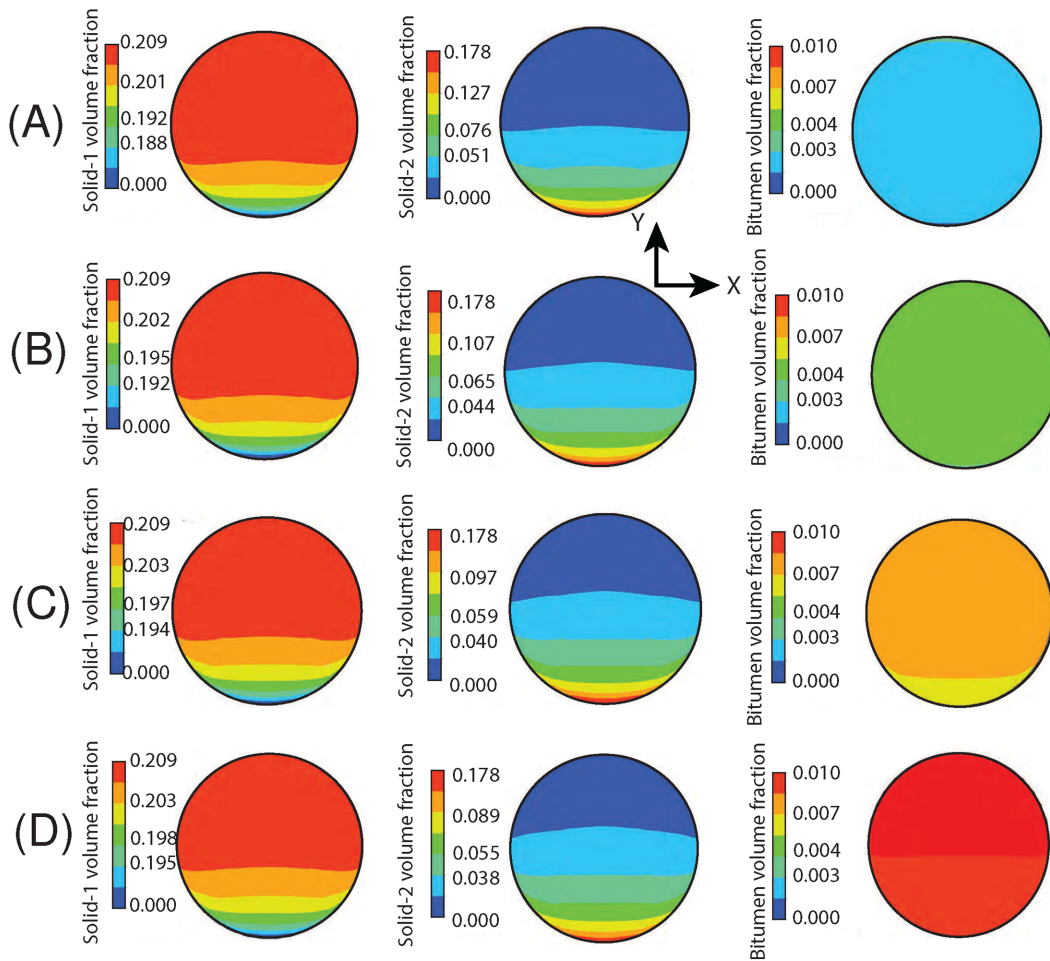


FIG. 8. The contour of solid and bitumen distributions. Bitumen fraction: (a) 0.0025, (b) 0.005, (c) 0.0075, and (d) 0.01 at a fixed bitumen fraction 0.0025 and a bitumen droplet size of $400\ \mu\text{m}$.

to an increase in the viscosity of the slurry system compared to the lower bitumen composition. However, the change in coarse solid (i.e., solid-2) fraction distribution clearly evident from Figs. 8(a) and 8(d). Notably, the concentration profile of fine particles displays a distribution trend opposite to that of coarse particles with an increase in bitumen droplet size.

Figures 8(a)–8(d) contours also show the bitumen fraction distribution across the pipe at $Z = 100\ \text{m}$ by altering the initial bitumen fraction up to 0.01. The bitumen distribution is significantly higher above the pipe center and gradually decreases from the center to the bottom part of the pipe. With an increase in the bitumen fraction, the results demonstrate the presence of bitumen droplets at the bottom of the pipe. The maximum distribution observed for higher bitumen fraction composition may be due to an increased particle–bitumen interaction in the domain and also leads increase in coarse particle distribution.

Figure 9 illustrates the quantitative analysis of flow profiles and pressure drop for different bitumen fraction conditions by keeping all other conditions similar. It can be seen that with an increased bitumen fraction carrier velocity profile slightly changed due to the change in

viscosity of the slurry system and particle–bitumen interactions. The presence of a higher bitumen fraction corresponds to more bitumen droplets in the slurry system due to higher turbulence characteristics. As a result, the velocity magnitude is relatively higher in the center of the pipe for a higher bitumen fraction compared to other conditions. However, the velocity profiles reveal that top and bottom parts of the pipe, the velocity distribution is more symmetrical, as shown in Fig. 9(a).

In Fig. 9(b), the chord-averaged solid fraction is presented to evaluate the effect of the bitumen fraction. The results indicated that the solid fraction profile gradually decreased from the top part of the pipe to the bottom part. As stated earlier, the gravitational force acting on coarse particles leads to accumulation at the bottom of the pipe along with small particles due to particle–particle interactions. It is worth noting that the solid fraction distribution slightly decreased near the wall with an increase in the bitumen fraction. This is in accord with the solids fraction distribution information across the pipe at $Z = 100\ \text{m}$ as depicted in Fig. 8. The results show that secondary phase interactions strongly influence the solid particle distribution in highly turbulent and viscous flows.

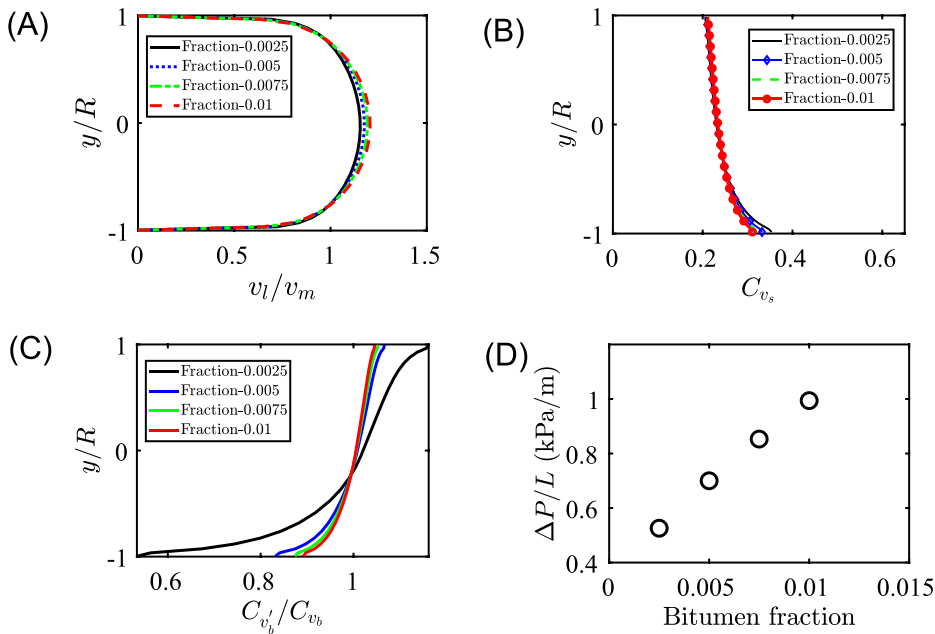


FIG. 9. Effect of bitumen fraction on (a) velocity profiles, (b) chord-average total solid concentration profiles, (c) bitumen distribution plots, and (d) pressure drop at a fixed bitumen fraction of 0.0025 and a bitumen droplet size of 400 μm .

Figure 9(c) provides an analysis of the bitumen distribution for different ranges of bitumen fractions. It is found that with an increase in the bitumen fraction, the distribution is more homogeneous in the system. However, for smaller bitumen fraction cases, a noticeable difference is observed in the bitumen fraction profiles from the top to the bottom of the pipe. In the case of lower fractions, more bitumen is accumulated at the top part of the pipe due to less interaction between solid particles and bitumen droplets. However, the bitumen fraction distribution is significantly lowered at the bottom of the pipe. On the other hand, for higher bitumen fraction cases, the bitumen distribution is slightly higher at the bottom of the pipe compared to lower bitumen fraction cases.

In addition, the pressure drop is also analyzed for all the conditions. Figure 9(d) demonstrates the pressure drop for different bitumen fractions by keeping other conditions, and bitumen droplet sizes are constant. It is profound that the increase in bitumen fraction significantly contributes to increase in pressure drop of the system. The particle–particle interaction and particle–bitumen interactions tend to concentrate more intensively from the top to bottom part of the pipe. Another possible explanation for this change in pressure drop is that the viscosity of the slurry system can also change with bitumen fraction. The increase in pressure drop resulted in an increase in specific power consumption and eventually more pumping cost in the industrial scale slurry transport in pipelines.

C. Effect of bubble size

This section discusses the influence of gas bubble size in the slurry system for fixed conditions. Different sizes of gas bubbles are considered ranging from 5 to 1000 μm based on the available experimental data. To understand the effect of bubble size on flow characteristics, bubble fraction is considered similar to bitumen fraction, as mentioned in Table I case-A. Figure 10 shows the distribution of

bubbles and bitumen droplets along the Z-length of the channel for two cases. All the analyses are performed after reaching the stable flow, and the flow time is at 200 s. The simulation results demonstrate that the gas bubble gradually moved to the pipe’s top part along the pipe’s length, as shown in Fig. 10(a). However, it is evident from Fig. 10(b) that the bitumen droplets are uniformly distributed at the inlet, and the bitumen droplets segregation gradually changes along with the length of the channel. Due to the smaller contact area between the tiny bubble and the particle, tiny bubbles attach to particles/droplets more easily and faster than larger bubbles.²⁸

The evolution of bitumen droplets is relatively high in the middle of the pipe, where $Z = 75$ m, and the bitumen is distributed from the top to the bottom part of the pipe. Near the outlet, most of the bitumen is accumulated at the top in a specific region due to bubble–bitumen interactions and particle–bitumen interactions. Importantly, a similar phenomenon is observed when the bubble size is 1000 μm , but the gas bubbles are accumulated at the top part of the pipe in one specific region. Figure 10(c) displays the gradual change in bubble distribution along the length of the channel. The results clearly show that minimal gas bubble distribution is observed from the center to the bottom part of the pipe, significantly different from the smaller bubble size case distributions. Recently, experimental work of Rosas *et al.*⁸² reported that the smaller dispersed bubbles remain stable in the complex slurry system since the buoyance forces are not sufficient to overcome the turbulent forces when the bubble diameter is sufficiently small. The numerical findings also corroborated with the work by Rosas *et al.*⁸² for different bubble sizes as shown in Figs. 10(a) and 10(c). In other words, the gravitational force that acts on the small bubbles is negligible compared to large-size bubbles. In the case of large-size bubbles, the buoyance forces are more prominent to overcome the turbulence forces. The bitumen distribution trend for a larger bubble is very similar to the 5 μm bubble case, as displayed in Fig. 10(d).

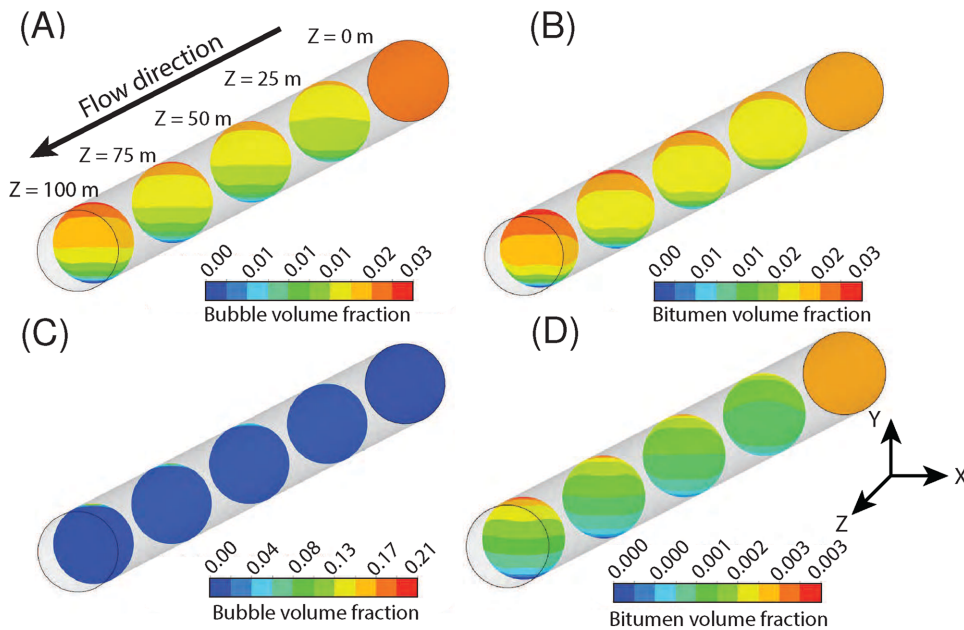


FIG. 10. (a) Bubble distribution and (b) bitumen distribution for $5\ \mu\text{m}$ bubble size. (c) Bubble distribution and (d) bitumen distribution for $1000\ \mu\text{m}$ bubble size at a fixed bitumen and bubble fraction 0.0025 and bitumen droplet size $400\ \mu\text{m}$.

To further understand the influence of gas bubbles, flow profiles, and pressure drop are quantified, as shown in Fig. 11. For all the cases, carrier velocity profiles showed a negligible change as shown in Fig. 11(a). It can be seen from Fig. 11(b) that for all the cases, chord-average total solid concentration profiles are similar. This suggests that bubble size has a negligible effect on solid concentration profiles for the considered range of bubble fractions. It is imperative to mention

that concentration profiles are similar, but small and coarse particle distributions may differ for similar conditions.

Figure 11(c) depicts the bitumen distribution profiles at the centerline of the plane for different bubble sizes. It is qualitatively perceptible that the amount of bitumen is relatively higher for larger bubbles and gradually to a minimum value. It is worth noting that the bitumen distribution profiles are similar for both 500 and $1000\ \mu\text{m}$ bubble sizes.

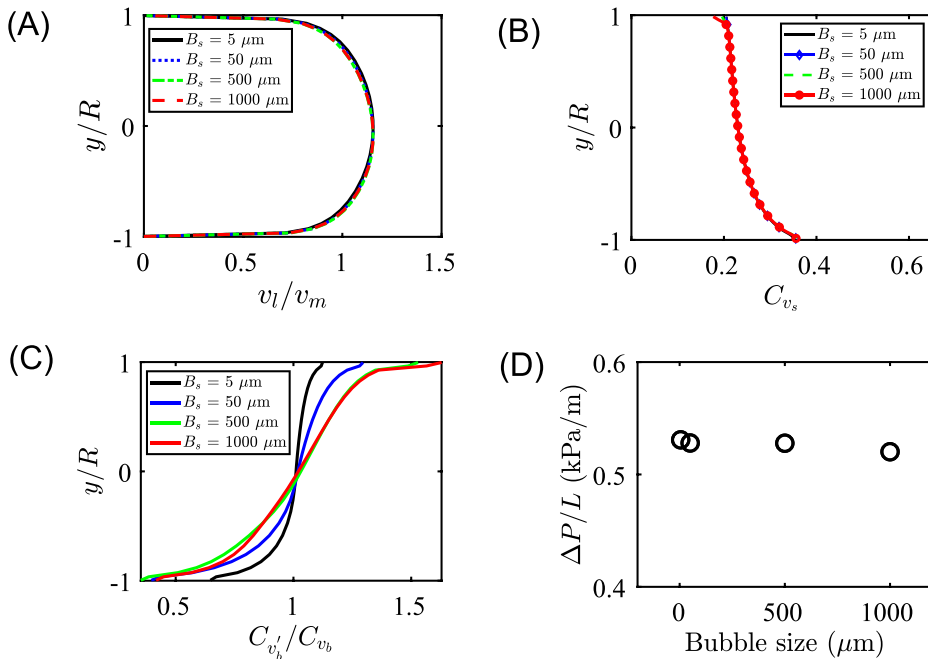


FIG. 11. Effect of bubble size (a) velocity profiles, (b) chord-average total solid concentration profiles, (c) bitumen distribution plots, and (d) pressure drop under fixed operation conditions. B_s denotes the bubble size.

However, it is important to notice that for smaller bubble sizes 5 and 50 μm case, the amount of bitumen is lower at the pipe's top part compared to larger bubbles. Booth⁸³ also reported a similar observation on the role of these tiny bubbles in accelerating particle–bubble/droplet attachment and improving recovery. Therefore, the bubble size also plays a significant role in the bitumen distribution in the pipe for efficient recovery. Notably, this finding indicated a strong synergy between bubbles and particles/bitumen droplets. On the other hand, the pressure drop decreased with an increase in bubble size, as shown in Fig. 11(d).

D. Effect of bubble fraction

This section demonstrates the effect of bubble formation on the pipeline's bitumen and gas bubble distribution. Numerical simulations are conducted at bubble fractions ranging from 0.0025 to 0.03 by considering the fixed bubble size of 500 μm and bitumen droplet size of 400 μm . Figure 12 shows the influence of bubble fraction on the carrier velocity, bitumen, and bubble distribution along the flow directions. It can be seen from Fig. 12(a) that the carrier velocity distribution gradually changed toward the outlet. The carrier velocity profile reaches stable flow and developed flow profile conditions after reaching critical length $Z = 75\text{ m}$.

The maximum velocity distribution is at the center of the pipe after reaching the critical length. The particle–particle collision and turbulent dispersion of particle clusters near the top wall result in a steep velocity gradient from the wall to the center region. In line with

previous observations, the maximum amount of bitumen is accumulated on the top part of the pipe, and the distribution gradually decreases from the top to the bottom part of the pipe as displayed in Fig. 12(b). Gas bubbles also accumulated at the upper part of the pipe in a specific region, as shown in Fig. 12(c). In contrast, with an increased bubble fraction, the carrier velocity distribution is shifted to the bottom side of the pipe, and the upper portion velocity magnitude range is relatively low. It could be attributed to an increase in bubble fraction since bitumen, bubbles, and fine particles are accumulated in the upper region, as demonstrated in Fig. 12(d).

Similar to the results from smaller bubble fractions, with an increase in bubble fraction under fixed conditions, the bitumen and bubble distribution are identical with a change maximum fraction range at the upper part of the pipe. The higher number of bubbles in the domain is due to a change in bubble fraction. Consequently, the higher number of bubbles critically impacts the bitumen accumulation at the top part of the pipe, as depicted in Fig. 12(e). It is evident from Fig. 12(f) that the bubble distribution is significantly different from the smaller bubble fraction case. With an increased bubble fraction, most bubbles are accumulated at the top and distributed to the center of the pipe. Figures 13(a)–13(d) also shows the three-dimensional view of particle and bitumen distribution across the different cross sections from the inlet to the outlet. It can be observed from Fig. 13(a) that small particle accumulation reached a stable flow pattern, and also along the length, coarse particle accumulation increased until $Z = 100\text{ m}$ [Fig. 13(b)]. The corresponding small particle velocity developed a fully developed flow

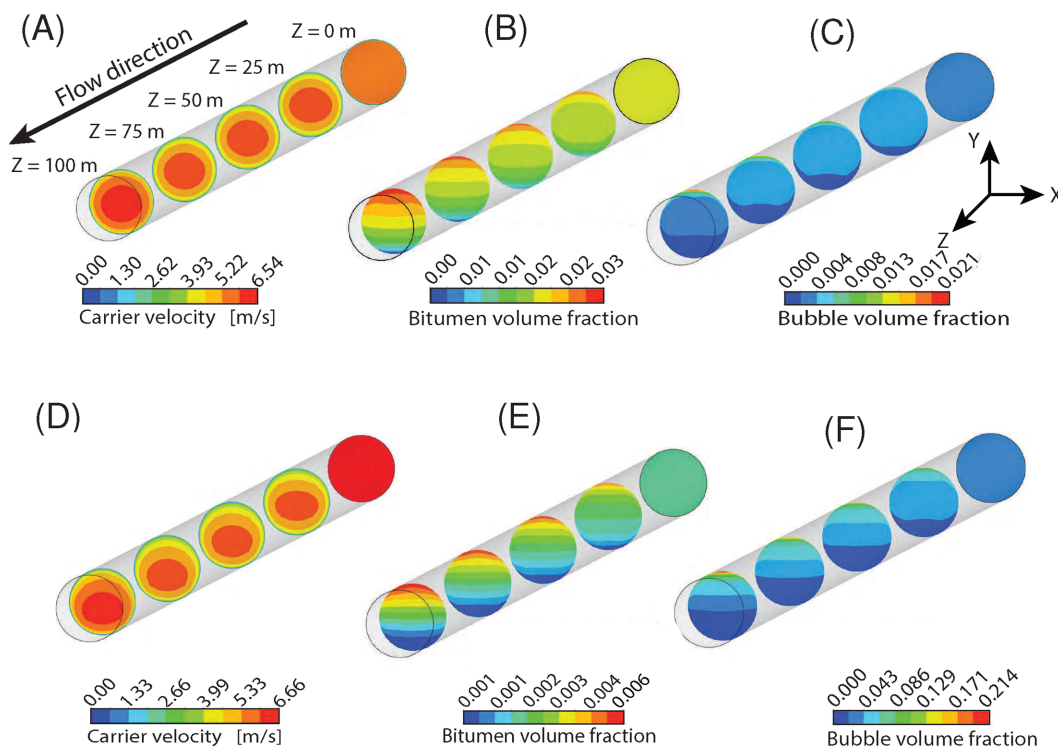


FIG. 12. (a) Carrier velocity distribution, (b) bitumen distribution, and (c) bubble distribution for the bubble fraction of 0.0025 at a fixed bubble size of 500 μm . (d) Carrier velocity distribution, (e) bitumen distribution, and (f) bubble distribution for the bubble fraction of 0.03 at a fixed bubble size of 500 μm .

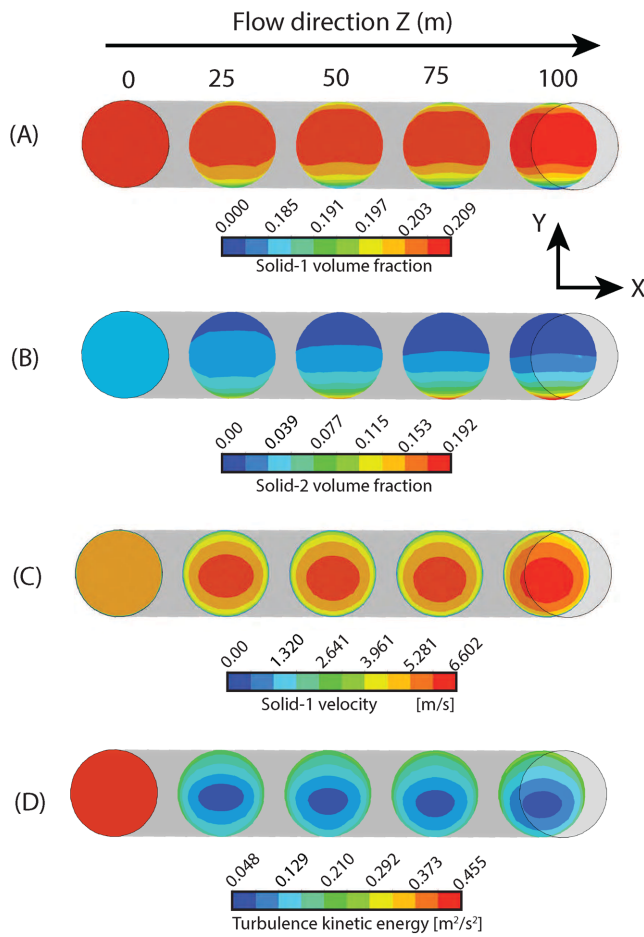


FIG. 13. (a) solid-1 fraction, (b) solid-2 fraction, (c) solid-1 velocity, and (d) turbulence kinetic energy distribution along the Z-direction for the bubble fraction of 0.01 and the bubble size of 500 μm .

condition near the outlet, as shown in Fig. 13(c), and turbulence kinetic energy also slightly increased along the flow direction [Fig. 13(d)].

Figure 14(a) demonstrates the effect of bubble fraction on carrier velocity profile across the vertical centerline for different bubble fraction conditions. A change in velocity profiles is observed with an increase in bubble fraction from 0.0025 to 0.03. At a higher bubble fraction, the carrier velocity profile is shifted slightly downward for the channel, and the velocity magnitude is relatively higher at the bottom part of the pipe. This is mainly due to the number of gas bubbles and bitumen droplets being greater at the top part of the pipe, which leads to a higher velocity magnitude at the bottom part of the pipe. For different bubble fraction conditions, Fig. 14(b) shows similar trends in solid volume fraction profiles. With an increase in bubble fraction, the top part of the pipe solids concentration decreased compared to conditions with a lower bubble fraction. Specifically, this is due to a higher concentration of bubbles and bitumen droplets.

Subsequently, the frequency of random collision increases during the movement of bubbles and droplets along with small particles to the top part of the pipe. The accumulation of particles with droplets and

bubbles enhances the interactions and promotes the distribution of bitumen at the top part of the pipe. As displayed in Fig. 14(c), bitumen profiles appear significantly altered with higher bubble fractions. Higher bubble fractions result in maximum bitumen accumulation and a linear decrease in the bitumen profile from top to bottom. At higher bubble fractions, the number of gas bubbles is comparatively higher, and the frequency of bubble-bitumen interactions is also accelerated, which causes bitumen to accumulate at the top of the pipe. The pressure drop with a higher bubble fraction, as shown in Fig. 14(d).

To understand the influence of gas bubble size and fraction on bitumen recovery, for all the systematic numerical investigations, bitumen recovery is estimated at $Z = 100$ m. A vertical centerline is considered on the cross section plane, and bitumen fraction recovery is estimated at different levels from top to bottom of the pipe specified in Table IX. The bitumen recovery is found to increase with increased bitumen droplet size, and from the top to the middle of the pipe, the maximum bitumen recovery is approximately 55%. However, the bitumen recovery greatly improved to approximately 80%. The optimum bitumen droplet size of 400 μm showed maximum bitumen recovery for the considered operating conditions. The higher bitumen fraction negatively impacted bitumen recovery from 54.32% to 51.35% for the top 50% cross section. Thus, the optimum bitumen fraction of 0.0025 showed maximum recovery under the fixed operating conditions.

Furthermore, bitumen recovery is also assessed with various gas bubble sizes, and the optimum bubble size is determined to be 500 μm . The maximum bitumen recovery of 59% could be observed for 500 μm , and a subsequent increase in bubble size bitumen recovery marginally decreased. The bubble fraction showed a significant effect on bitumen recovery with the bubble size of 500 μm . With an increase in bubble fraction, the bitumen recovery increased from a lower value of 59%–80%. Therefore, CFD results demonstrate the bubble fraction plays a critical role in the bitumen recovery for the considered conditions.

VI. CONCLUSIONS

In this work, we employ a three-dimensional, transient Eulerian CFD model to study the flow behavior of complex multiphase slurry systems. Four-phases of non-Newtonian tailings slurry flow with bitumen droplets and bubbles in an industrial pipeline are modeled. The CFD model is validated with industrial field data for six sets in terms of the velocity profile and pressure drop with a maximum error of 6% and <10%. A detailed sensitivity analysis is demonstrated on the selection of carrier–solid and solid–bitumen drag models. The combination of small and large particle sizes (i.e., 75 and 700 μm) and bitumen droplet size (i.e., 400 μm) provided good agreement with field data in velocity profile and pressure drop.

Our numerical findings reveal that the bitumen droplet size plays a significant role in the bitumen distribution, and larger droplets accumulate at the top part of the pipe. Bitumen droplet size strongly influences bitumen distribution profiles. With an increase in bitumen fraction, solid concentration profiles slightly shifted, and pressure drop increased. This study revealed that with an increase in bitumen fraction, pressure drop increased, and bitumen distribution profiles also showed significant differences due to a change in the slurry composition. However, the coarse particle distribution also changed with an increase in the bitumen fraction from 0.0025 to 0.01. The results indicate that with an increase in the bubble size, the bitumen distribution

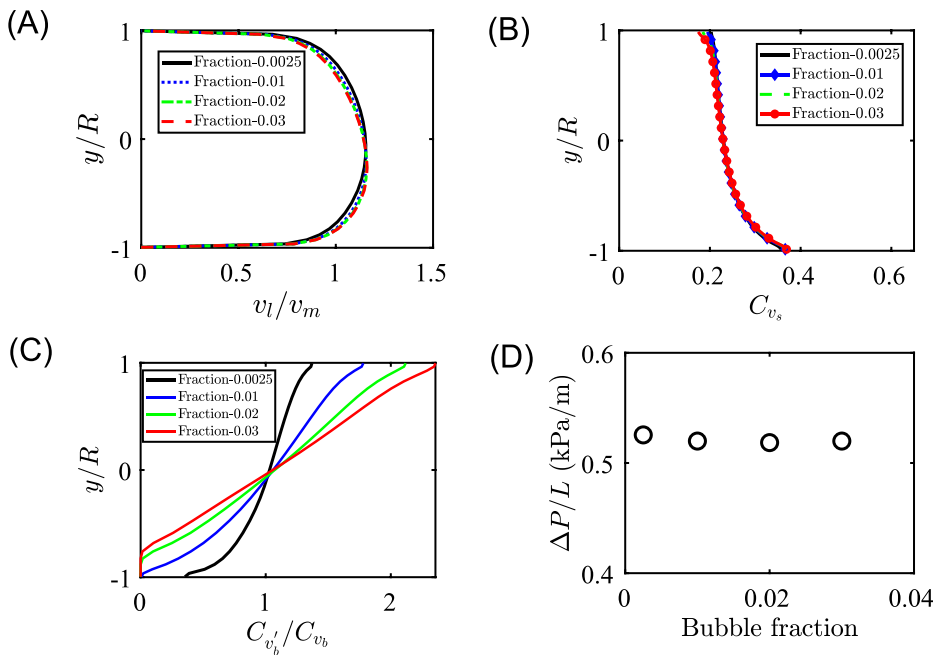


FIG. 14. Effect of the bubble fraction on (a) velocity profiles, (b) chord-average total solid concentration profiles, (c) bitumen distribution plots, and (d) pressure drop under fixed operation conditions.

TABLE IX. Bitumen recovery summary.

Study	Parameter range	Bitumen recovery percentage		
		Top 25%	Top 50%	Top 75%
Bitumen droplet size (μm)	100	27.70	52.68	78.15
	200	27.91	52.93	78.39
	300	28.34	53.49	78.90
	400	28.98	54.32	79.66
Bitumen fraction	0.0025	28.98	54.32	79.66
	0.005	27.31	51.91	77.13
	0.0075	27.06	51.54	76.76
	0.01	26.93	51.35	76.57
Bubble size (μm)	5	27.97	52.75	78.24
	50	30.36	55.82	81.04
	500	32.78	59.03	83.22
	1000	32.80	58.70	82.43
Bubble fraction	0.0025	32.78	59.03	83.22
	0.01	39.72	68.52	90.64
	0.02	45.65	76.22	95.78
	0.03	49.32	80.51	97.68

effectively improved, and the optimum bubble size is noted as $500 \mu\text{m}$. Higher bubble fractions showed a strong influence on velocity and concentration profiles. The optimum conditions for higher bitumen recovery are revealed by CFD results in the pipeline.

The developed CFD model provides a powerful tool for understanding the complex multiphase flow behaviors during highly turbulent and viscous slurry transport. Therefore, this work contributes

toward accurate predictions that may guide the process design of an industrial-scale slurry transport. The outcomes of these studies are likely to guide conditions for bitumen recovery from tailings slurries.

ACKNOWLEDGMENTS

The authors acknowledge the funding support from the Institute for Oil Sands Innovation (IOSI) [Project IOSI 2019-04 (TA)] and from the Natural Science and Engineering Research Council of Canada (NSERC)-Alliance. This research was undertaken, in part, thanks to funding from the Canada Research Chairs Program. We also thank Compute Canada (www.computecanada.ca) for continued support through extensive access to the Compute Canada HPC Cedar and Graham clusters.

AUTHOR DECLARATIONS

Conflict of Interest

The authors have no conflicts to disclose.

Author Contributions

Somasekhara Goud Sontti: Conceptualization (lead); Formal analysis (lead); Investigation (lead); Methodology (lead); Software (lead); Validation (lead); Visualization (lead); Writing – original draft (lead); Writing – review & editing (lead). **Mohsen Sadeghi:** Validation (equal); Writing – review & editing (equal). **Kaiyu Zhou:** Data curation (equal). **Enzu Zheng:** Writing – review & editing (equal). **Xuehua Zhang:** Conceptualization (lead); Funding acquisition (lead); Methodology (equal); Project administration (lead); Resources (lead); Supervision (lead); Writing – review & editing (equal).

DATA AVAILABILITY

The data that support the findings of this study are available from the corresponding author upon reasonable request.

NOMENCLATURE

C_{fr}	friction coefficient between solid phases (–)
C_v	chord-averaged concentration (–)
D	pipe diameter (L)
d_p	particle diameter (L)
e	restitution coefficient (–)
f_{drag}	drag function (–)
g	gravitational acceleration ($L T^{-2}$)
g_0	radial distribution function (–)
i	hydraulic gradient (–)
I_{2D}	second invariant of the deviatoric stress tensor (–)
k	turbulent kinetic energy ($L^2 T^{-2}$)
K_{fs}	momentum exchange coefficient between fluid
p	locally-averaged pressure ($M L^{-1} T^{-2}$)
R	pipe radius (L)
t	time (T)
v	velocity ($L T^{-1}$)
V	velocity ($L T^{-1}$)
$ \vec{v}'_s $	fluctuating solids velocity ($L T^{-1}$)
x	horizontal coordinate (L)
y	vertical coordinate (L)
z	axial coordinate (L)
ΔP	area-averaged gauge pressure ($M L^{-1} T^{-2}$)

Greek symbol

α	locally-averaged volume fraction (–)
$\alpha_{s,max}$	maximum packing limit (–)
$\dot{\gamma}$	shear strain rate (T^{-1})
γ_{Θ_s}	collisional dissipation of energy (E)
η	apparent viscosity ($M L^{-1} T^{-1}$)
η_t	turbulent diffusivity (–)
Θ	granular temperature ($L^2 T^{-2}$)
μ	dynamic viscosity ($M L^{-1} T^{-1}$)
ρ	density ($M L^{-3}$)
τ	shear stress ($M L^{-1} T^{-2}$)
ϕ	angle of internal friction (–)
ϕ_{fs}	the energy exchange between the fluid and the solid phases (E)

Subscripts

col	collisional part of viscosity
fr	frictional part of viscosity
kin	kinetic part of viscosity
l	liquid
p	p th solid phase
q	q th solid phase
s	solid
ss	solid particles

REFERENCES

1. Pullum, D. V. Boger, and F. Sofra, "Hydraulic mineral waste transport and storage," *Annu. Rev. Fluid Mech.* **58**, 157 (2018).
2. M. Mohaibes and H. Heinonen-Tanski, "Aerobic thermophilic treatment of farm slurry and food wastes," *Bioresour. Technol.* **95**, 245 (2004).
3. R. Cepuritis, S. Jacobsen, S. Smeplass, E. Mortzell, B. J. Wigum, and S. Ng, "Influence of crushed aggregate fines with micro-proportioned particle size distributions on rheology of cement paste," *Cem. Concr. Compos.* **80**, 64 (2017).
4. N. Cruz, J. Forster, and E. R. Bobicki, "Slurry rheology in mineral processing unit operations: A critical review," *Can. J. Chem. Eng.* **97**, 2102 (2019).
5. R. Xiong, J. H. Plette, Z. Zhang, J. Guo, and S. G. Hatzikiriakos, "Effect of asphaltene on the rheological properties of bitumen," *Phys. Fluids* **34**, 083111 (2022).
6. C. A. Shook and M. C. Roco, *Slurry Flow: Principles and Practice* (Elsevier, 2015).
7. A. Uzi and A. Levy, "Flow characteristics of coarse particles in horizontal hydraulic conveying," *Powder Technol.* **326**, 302 (2018).
8. P. Enos, "Flow regimes in debris flow," *Sedimentology* **24**, 133 (1977).
9. A. Pokharel, V. Akkerman, I. B. Celik, R. L. Axelbaum, A. Islas, and Z. Yang, "Impact of particle loading and phase coupling on gas–solid flow dynamics: A case study of a two-phase, gas–solid flow in an annular pipe," *Phys. Fluids* **33**, 073308 (2021).
10. S. Parvathaneni and V. V. Buwa, "Role of bubbling behaviour in segregation and mixing of binary gas–solids flow of particles with different density," *Powder Technol.* **372**, 178 (2020).
11. S. Crosby, R. Fay, C. Groark, J. R. Smith, T. Sullivan, R. Pavia, G. Shigenaka *et al.*, Technical Memorandum (2013), <https://repository.library.noaa.gov/view/noaa/2670>
12. Q. Kang, S. Song, J. Yu, B. Shi, Y. Chen, X. Lv, Y. Liu, Z. Bai, B. Hong, W. Wang *et al.*, "Simulation of upward gas–hydrate slurry multiphase flow in a vertical concentric annulus for natural gas hydrate solid fluidization exploitation," *Phys. Fluids* **33**, 103102 (2021).
13. C. C. Small, S. Cho, Z. Hashisho, and A. C. Ulrich, "Emissions from oil sands tailings ponds: Review of tailings pond parameters and emission estimates," *J. Pet. Sci. Eng.* **127**, 490 (2015).
14. H. Khademi, A. Abbaspour, S. Martinez-Martinez, M. Gabarron, V. Shahrokh, A. Faz, and J. A. Acosta, "Provenance and environmental risk of windblown materials from mine tailing ponds, Murcia, Spain," *Environ. Pollut.* **241**, 432 (2018).
15. B. Nimana, C. Canter, and A. Kumar, "Energy consumption and greenhouse gas emissions in the recovery and extraction of crude bitumen from Canada's oil sands," *Appl. Energy* **143**, 189 (2015).
16. Y. B. Dibike, A. Shakibaenia, I. G. Droppo, and E. Caron, "Modelling the potential effects of oil-sands tailings pond breach on the water and sediment quality of the lower Athabasca River," *Sci. Total Environ.* **642**, 1263 (2018).
17. R. Gillies, M. McKibben, and C. Shook, "Pipeline flow of gas, liquid and sand mixtures at low velocities," *J. Can. Pet. Technol.* (published online, 1997).
18. D. Scott and P. Rao, "Transport of solids by gas-liquid mixtures in horizontal pipes," *Can. J. Chem. Eng.* **49**, 302 (1971).
19. T. Fukuda and Y. Shoji, "Pressure drop and heat transfer for tree phase flow: 1st report, flow in horizontal pipes," *Bull. JSME* **29**, 3421 (1986).
20. A. A. Zahid, S. Raza ur Rehman, S. Rushd, A. Hasan, and M. A. Rahman, "Experimental investigation of multiphase flow behavior in drilling annuli using high speed visualization technique," *Front. Energy Res.* **14**, 635 (2020).
21. D. Kaushal, K. Sato, T. Toyota, K. Funatsu, and Y. Tomita, "Effect of particle size distribution on pressure drop and concentration profile in pipeline flow of highly concentrated slurry," *Int. J. Multiphase Flow* **31**, 809 (2005).
22. V. Wallwork, Z. Xu, and J. Masliyah, "Bitumen recovery with oily air bubbles," *Can. J. Chem. Eng.* **81**, 993 (2003).
23. A. Motamed Dashliborun, J. Zhou, P. Esmaeili, and X. Zhang, "Microbubble-enhanced recovery of residual bitumen from the tailings of oil sands extraction in a laboratory-scale pipeline," *Energy Fuels* **34**, 16476 (2020).
24. K. Zhou, S. G. Sontti, J. Zhou, P. Esmaeili, and X. Zhang, ChemRxiv.
25. V. Wallwork, Z. Xu, and J. Masliyah, "Processibility of Athabasca oil sand using a laboratory hydro transport extraction system (LHES)," *Can. J. Chem. Eng.* **82**, 687 (2004).

- ²⁶Y. Xing, X. Gui, L. Pan, B.-E. Pinchasik, Y. Cao, J. Liu, M. Kappl, and H.-J. Butt, "Recent experimental advances for understanding bubble-particle attachment in flotation," *Adv. Colloid Interface Sci.* **246**, 105 (2017).
- ²⁷H. Wang, W. Yang, X. Yan, L. Wang, Y. Wang, and H. Zhang, "Regulation of bubble size in flotation: A review," *J. Environ. Chem. Eng.* **8**, 104070 (2020).
- ²⁸J. Z. Zhou, H. Li, R. S. Chow, Q. Liu, Z. Xu, and J. Masliyah, "Role of mineral flotation technology in improving bitumen extraction from mined Athabasca oil sands. II. Flotation hydrodynamics of water-based oil sand extraction," *Can. J. Chem. Eng.* **98**, 330 (2020).
- ²⁹Y. Li, F. Wu, W. Xia, Y. Mao, Y. Peng, and G. Xie, "The bridging action of microbubbles in particle-bubble adhesion," *Powder Technol.* **375**, 271 (2020).
- ³⁰Y. Gao, A. M. Dashliborun, J. Z. Zhou, and X. Zhang, "Formation and stability of cavitation microbubbles in process water from the oilsands industry," *Ind. Eng. Chem. Res.* **60**, 3198 (2021).
- ³¹B. Albijanic, O. Ozdemir, A. V. Nguyen, and D. Bradshaw, "A review of induction and attachment times of wetting thin films between air bubbles and particles and its relevance in the separation of particles by flotation," *Adv. Colloid Interface Sci.* **159**(1), 1 (2010).
- ³²C. Qiao, D. Yang, X. Mao, L. Xie, L. Gong, X. Peng, Q. Peng, T. Wang, H. Zhang, and H. Zeng, "Recent advances in bubble-based technologies: Underlying interaction mechanisms and applications," *Appl. Phys. Rev.* **8**, 011315 (2021).
- ³³G. V. Messa, Q. Yang, O. E. Adedeji, Z. Chára, C. A. R. Duarte, V. Matoušek, M. G. Rasteiro, R. S. Sanders, R. C. Silva, and F. J. de Souza, "Computational fluid dynamics modelling of liquid–solid slurry flows in pipelines: State-of-the-art and future perspectives," *Processes* **9**, 1566 (2021).
- ³⁴Y. Zhang, X.-B. Lu, and X.-H. Zhang, "An optimized Eulerian–Lagrangian method for two-phase flow with coarse particles: Implementation in open-source field operation and manipulation, verification, and validation," *Phys. Fluids* **33**, 113307 (2021).
- ³⁵D. Kaushal, T. Thinglas, Y. Tomita, S. Kuchii, and H. Tsukamoto, "CFD modeling for pipeline flow of fine particles at high concentration," *Int. J. Multiphase Flow* **43**, 85 (2012).
- ³⁶M.-Z. Li, Y.-P. He, Y.-D. Liu, and C. Huang, "Hydrodynamic simulation of multi-sized high concentration slurry transport in pipelines," *Ocean Eng.* **163**, 691 (2018).
- ³⁷M. Li, Y. He, Y. Liu, and C. Huang, "Effect of interaction of particles with different sizes on particle kinetics in multi-sized slurry transport by pipeline," *Powder Technol.* **338**, 915 (2018).
- ³⁸M. Zhang, Y. Kang, W. Wei, D. Li, and T. Xiong, "CFD investigation of the flow characteristics of liquid–solid slurry in a large-diameter horizontal pipe," *Part. Sci. Technol.* **39**, 712 (2021).
- ³⁹H. Shi, J. Yuan, and Y. Li, "The impact of swirls on slurry flows in horizontal pipelines," *J. Mar. Sci. Eng.* **9**, 1201 (2021).
- ⁴⁰A. Fluent, *ANSYS fluent 20.0 user's guide*, ANSYS FLUENT Inc., 2020.
- ⁴¹T. Fonty, M. Ferrand, A. Leroy, A. Joly, and D. Violeau, "Mixture model for two-phase flows with high density ratios: A conservative and realizable SPH formulation," *Int. J. Multiphase Flow* **111**, 158 (2019).
- ⁴²J. Ling, P. Skudarnov, C. Lin, and M. Ebadian, "Numerical investigations of liquid–solid slurry flows in a fully developed turbulent flow region," *Int. J. Heat Fluid Flow* **24**, 389 (2003).
- ⁴³M.-Z. Li, Y.-P. He, Y.-D. Liu, and C. Huang, "Pressure drop model of high-concentration graded particle transport in pipelines," *Ocean Eng.* **163**, 630 (2018).
- ⁴⁴E. Zheng, M. Rudman, S. Kuang, and A. Chryst, "Turbulent coarse-particle non-Newtonian suspension flow in a pipe," *Int. J. Multiphase Flow* **142**, 103698 (2021).
- ⁴⁵S. Javadi, R. Gupta, S. Bhattacharya, and P. Slatter, "Laminar flow of non-Newtonian thickened tailings slurry through an open channel," *Can. J. Chem. Eng.* **93**, 1922 (2015).
- ⁴⁶E. Zheng, M. Rudman, S. Kuang, and A. Chryst, "Dense non-Newtonian suspension flow: Effect of solids properties and pipe size," *AIChE J.* **68**(8), e17690 (2022).
- ⁴⁷S. Elghobashi, "Direct numerical simulation of turbulent flows laden with droplets or bubbles," *Annu. Rev. Fluid Mech.* **51**, 217 (2019).
- ⁴⁸C. Martínez-bazan, J. Montanes, and J. C. Lasheras, "On the breakup of an air bubble injected into a fully developed turbulent flow. II. Size PDF of the resulting daughter bubbles," *J. Fluid Mech.* **401**, 183 (1999).
- ⁴⁹C. Xing, T. Wang, K. Guo, and J. Wang, "A unified theoretical model for breakup of bubbles and droplets in turbulent flows," *AIChE J.* **61**, 1391 (2015).
- ⁵⁰J. T. Bulmer and T. E. Starr, *Synchrude Analytical Methods for Oil Sand and Bitumen Processing* (Alberta Oil Sands Technology and Research Authority, 1979), 173 pp, <https://books.google.ca/books?id=gBUKHAACAIAJ>
- ⁵¹M. Sadeghi, S. G. Sontti, E. Zheng, and X. Zhang, [arXiv:2209.00079](https://arxiv.org/abs/2209.00079) (2022).
- ⁵²R. Maron, M. Fernald, C. O'Keefe, J. Viega, and T. Bailey, "New applications of SONAR-based technology in the minerals processing industry: Velocity profile measurement and pipe wall wear monitoring in hydrotransport lines," Technical Paper No. BI0351 (2008), <https://www.cidra.com/resource-center/sonar-based-technology-velocity-profile-measurement-pipewall-wear-monitoring-hydrotransport-lines>
- ⁵³M. Sadeghi, S. Li, E. Zheng, S. G. Sontti, P. Esmaeili, and X. Zhang, "CFD simulation of turbulent non-Newtonian slurry flows in horizontal pipelines," *Ind. Eng. Chem. Res.* **61**, 5324 (2022).
- ⁵⁴S. Parvathaneni and V. V. Buwa, "Eulerian multifluid simulations of segregation and mixing of binary gas-solids flow of particles with different densities," *Chem. Eng. Sci.* **245**, 116901 (2021).
- ⁵⁵S. Parvathaneni, S. Karmakar, and V. V. Buwa, "Eulerian simulations of bubbling and jetting regimes in a fluidized bed," *Particuology* **75**, 50 (2023).
- ⁵⁶D. Gidaspow, R. Bezburuah, and J. Ding, "Hydrodynamics of circulating fluidized beds: Kinetic theory approach," Technical Report No. CONF-920502-1 and ON: DE92002879 (Illinois Institute of Technology, Chicago, IL, 1991), <https://www.osti.gov/biblio/5896246>
- ⁵⁷A. D. Burns, T. Frank, I. Hamill, J.-M. Shi *et al.*, in *Proceedings of the 5th International Conference on Multiphase Flow (ICMF)* (ICMF, 2004), Vol. 4, pp. 1–17.
- ⁵⁸X. Ting, S. A. Miedema, and C. Xiuhuan, "Comparative analysis between CFD model and DHLLDV model in fully-suspended slurry flow," *Ocean Eng.* **181**, 29 (2019).
- ⁵⁹C. L. Antaya, K. F. K. Adane, and R. S. Sanders, in *Proceedings of the Fluids Engineering Division Summer Meeting* (ASME, 2012), Vol. 1: Symposia, Parts A and B, p. 1659.
- ⁶⁰W. Liu, Y. He, M. Li, C. Huang, and Y. Liu, "Effect of drag models on hydrodynamic behaviors of slurry flows in horizontal pipes," *Phys. Fluids* **34**, 103311 (2022).
- ⁶¹B. E. Launder and D. B. Spalding, in *Numerical Prediction of Flow, Heat Transfer, Turbulence and Combustion* (Elsevier, 1983), pp. 96–116.
- ⁶²C. Katsamis, T. Craft, H. Iacovides, and J. C. Uribe, "Use of 2-D and 3-D unsteady RANS in the computation of wall bounded buoyant flows," *Int. J. Heat Fluid Flow* **93**, 108914 (2022).
- ⁶³J. Hu and T. Tao, "Numerical investigation of ice pigging isothermal flow in water-supply pipelines cleaning," *Chem. Eng. Res. Des.* **182**, 428 (2022).
- ⁶⁴K. Ma, Z. Liu, Y. Tang, X. Liu, Y. Yang, and S. Yang, "Numerical investigation on ice slurry flow in horizontal elbow pipes," *Therm. Sci. Eng. Prog.* **27**, 101083 (2022).
- ⁶⁵M. Abdulrahman, "Temperature profiles of a direct contact heat transfer in a slurry bubble column," *Chem. Eng. Res. Des.* **182**, 183 (2022).
- ⁶⁶A. K. Thakur, R. Kumar, N. Banerjee, P. Chaudhari, and G. K. Gaurav, "Hydrodynamic modeling of liquid-solid flow in polyolefin slurry reactors using CFD techniques—A critical analysis," *Powder Technol.* **405**, 117544 (2022).
- ⁶⁷K. Ro and H. Ryou, "Development of the modified k- ϵ turbulence model of power-law fluid for engineering applications," *Sci. China Technol. Sci.* **55**, 276 (2012).
- ⁶⁸O. B. Adeyinka, S. Samiei, Z. Xu, and J. H. Masliyah, "Effect of particle size on the rheology of Athabasca clay suspensions," *Can. J. Chem. Eng.* **87**, 422 (2009).
- ⁶⁹N. Sen, K. Singh, A. Patwardhan, S. Mukhopadhyay, and K. Shenoy, "CFD simulation of two-phase flow in pulsed sieve-plate column—Identification of a suitable drag model to predict dispersed phase hold up," *Sep. Sci. Technol.* **51**, 2790 (2016).
- ⁷⁰X. Zhang, G. J. Nathan, Z. F. Tian, and R. C. Chin, "The influence of the coefficient of restitution on flow regimes within horizontal particle-laden pipe flows," *Phys. Fluids* **33**, 123318 (2021).
- ⁷¹W. Liu, Y. He, M. Li, Q. Chen, Y. Liu, and C. Huang, "Computational fluid dynamics modeling of slurry flow in horizontal pipes: Effect of specular coefficient on hydraulic gradient," *Ocean Eng.* **238**, 109625 (2021).

- ⁷²L. Schiller and Z. Naumann, "A drag coefficient correlation," *Z. Deutsch. Ing.* **77**, 318 (1933).
- ⁷³S. A. Morsi and A. J. Alexander, "An investigation of particle trajectories in two-phase flow systems," *J. Fluid Mech.* **55**, 193–208 (1972).
- ⁷⁴R. Clift, J. R. Grace, and M. E. Weber, *Bubbles, Drops, and Particles* (Dover, 2005), https://books.google.ca/books/about/Bubbles_Drops_and_Particles.htm?id=UUrOmD8niUQC&redir_esc=y
- ⁷⁵T. Takamasa and A. Tomiyama, in Proceedings of the Ninth International Topical Meeting on Nuclear Reactor Thermal Hydraulics (NURETH) (1999).
- ⁷⁶M. Ishii, paper presented at the Department of Energy International Workshop on Two-phase Flow Fundamentals (1987).
- ⁷⁷K. Malysa, S. Ng, L. Cymbalista, J. Czarnecki, and J. Masliyah, "A method of visualization and characterization of aggregate flow inside a separation vessel. I. Size, shape and rise velocity of the aggregates," *Int. J. Miner. Process.* **55**, 171 (1999).
- ⁷⁸K. Malysa, S. Ng, J. Czarnecki, and J. Masliyah, "A method of visualization and characterization of aggregate flow inside a separation vessel. II. Composition of the bitumen–air aggregates," *Int. J. Miner. Process.* **55**, 189 (1999).
- ⁷⁹J. Wang, S. Wang, T. Zhang, and Y. Liang, "Numerical investigation of ice slurry isothermal flow in various pipes," *Int. J. Refrig.* **36**, 70 (2013).
- ⁸⁰A. Bordet, S. Poncet, M. Poirier, and N. Galanis, "Advanced numerical modeling of turbulent ice slurry flows in a straight pipe," *Int. J. Therm. Sci.* **127**, 294 (2018).
- ⁸¹G. V. Messa and V. Matousek, "Analysis and discussion of two fluid modelling of pipe flow of fully suspended slurry," *Powder Technol.* **360**, 747 (2020).
- ⁸²L. M. Rosas, C. L. Bassani, R. F. Alves, F. A. Schneider, M. A. Marcelino Neto, R. E. Morales, and A. K. Sum, "Measurements of horizontal three-phase solid-liquid-gas slug flow: Influence of hydrate-like particles on hydrodynamics," *AIChE J.* **64**, 2864 (2018).
- ⁸³R. B. Booth, "Flotation," *Ind. Eng. Chem. Res.* **46**, 105 (1954).